Fabrication and characterization of perpendicular magnetic anisotropy thin-film CoCrPt grown on a Ti underlayer

by

Margaret Marie Kane

Submitted to the
Department of Materials Science and Engineering
in Partial Fulfillment of the Requirements for the Degree of

Bachelor of Science

at the

Massachusetts Institute of Technology

June 2015

Signature of Author……………………….………………………………………………..........
Department of Materials Science and Engineering
05/01/2015

Certified by……………………………………………………………………………………
Caroline Ross
Toyota Professor of Materials Science and Engineering
Thesis Supervisor

Accepted by ……………………..……………………………………………………………
Geoffrey Beach
Class of '58' Associate Professor of Materials Science and Engineering
Chairman, Undergraduate Thesis Committee

Fabrication and characterization of perpendicular magnetic anisotropy thin-film CoCrPt grown on a Ti underlayer

by

Margaret Marie Kane

Submitted to the Department of Materials Science and Engineering on May 1, 2015
in Partial Fulfillment of the Requirements for the Degree of Bachelor of Science
in Materials Science and Engineering

ABSTRACT

CoCrPt has potential applications as a memory storage technology because of its perpendicular magnetic anisotropy (PMA) characteristics. An underlayer can be used to ensure the out-of-plane magnetization required for PMA functionalities. Ti, with a lattice constant of a = 2.95 Å can be used to encourage uniaxial c-axis growth in CoCrPt (lattice constant $a \cong 2.55$ Å, dependent on exact composition). In this report, varying thicknesses of Ti (t = 0, 20, 40, 60, 70, 80, 90, 100nm) and CoCrPt (t = 50, 75, 90, 100, 125, 150nm) were sputtered onto naturally oxidized silicon substrates. Using various characterization methods, these films were investigated in order to better understand the system. The exact composition of the CoCrPt films was found to be approximately $Co_{60.2}Cr_{16.4}Pt_{23.4}$, with a Curie temperature of about 600 ºC. The addition of a Ti underlayer resulted in an increase in coercivity to approximately 1250 Oe for $t >$ 60nm. However, switching field distribution and saturation magnetization appear to be independent of underlayer thickness. All samples show evidence of out-of-plane growth and the roughness of the films increases until it also plateaus at about t = 60nm. When CoCrPt thickness is varied on a constant Ti underlayer, the PMA properties of the materials decrease with increasing thickness due to increased disorder and potential relaxation of the lattice in thicker films. The switching field distribution shows a significant increase, implying that a thicker film has a more homogenous distribution of grain sizes. XRD peaks confirm out-of-plane growth and suggest a trend of increasing c lattice constant as the thickness of the film increases.

Thesis Supervisor: Caroline Ross
Title: Toyota Professor of Materials Science and Engineering

ACKNOWLEDGEMENTS

I would like to first thank Dr. Pin Ho and Professor Caroline Ross for their invaluable help with this thesis. Thank you Libby Shaw, Donald Galler, Kun-Hua Tu for training me to use the instruments instrumental to my completion of this thesis. I also need to thank all the professors and lab instructors I've had at MIT who both inspired me and taught me the skills I now use on a regular basis. Thanks to my parents and sisters for their support and love.

TABLE OF CONTENTS

Table of Figures

TABLE OF TABLES

INTRODUCTION

This project focuses on the fabrication and characterization of thin films of CoCrPt on Ti underlayers of varying thicknesses. Under certain conditions, CoCrPt exhibits perpendicular magnetic anisotropy (PMA), which is of interest for high-density data storage. PMA materials are widely used and have replaced materials that exhibit longitudinal magnetic anisotropy (LMA). LMA was the dominant technology in memory storage until recently, but it has a lower-density data storage capability because it requires larger domains. In some applications, however, it was advantageous, specifically those that recorded information linearly, like tapes (Figure 1a).

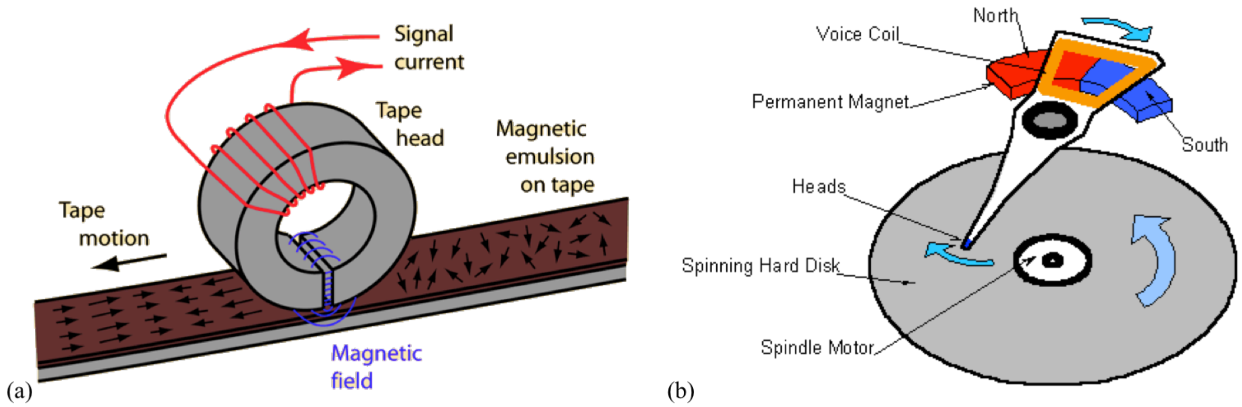

Figure 1. Recording medium geometries. (a) Tapes, linear recording; (b) modern hard drive, circumferential recording. Courtesy of hyperphysics and Ghandi Institute of Technology and Management.

However, floppy disks (now outdated) and modern hard drives (Figure 1b) use circumferential recording. In hard drives, the use of PMA would enable smaller bit sizes, increasing the data density.

New research and developments in memory storage technology also use PMA materials. For example, racetrack memory, a novel way of storing data where a current is passed through a wire, causing the domains therein to pass read and write heads. These stationary heads would interpret or manipulate the magnetization direction in a similar fashion to the current technology used to store data.

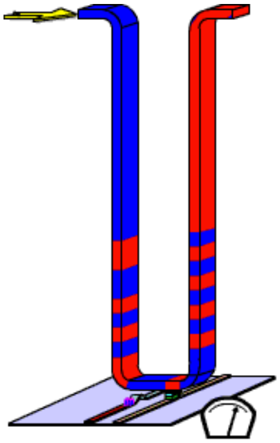

Figure 2. Racetrack memory schematic. Courtesy of IBM

Racetrack memory can potentially offer higher energy density storage than flash memory or disk drives and so is of great interest as a storage solution. The use of PMA materials in this application would allow for more efficient spin torque switching,

Another emerging technology that could benefit from the use of PMA is magnetic random access memory (MRAM). MRAM, unlike other types of RAM, is non-volatile, meaning that it will continue to store information without an external power source. To accomplish this non-volatility, MRAM stores information as an array of spin valves instead of electric charge (see Figure 3). A spin valve consists of two magnetic layers separated by a thin insulator. One of the two ferromagnets' directionality is fixed by an antiferromagnet and, by measuring the electrical resistance, one can ascertain the directionality of the un-fixed layer (parallel or antiparallel). Once again, a PMA material, in place of an LMA material, would increase the spin torque switching efficiency.

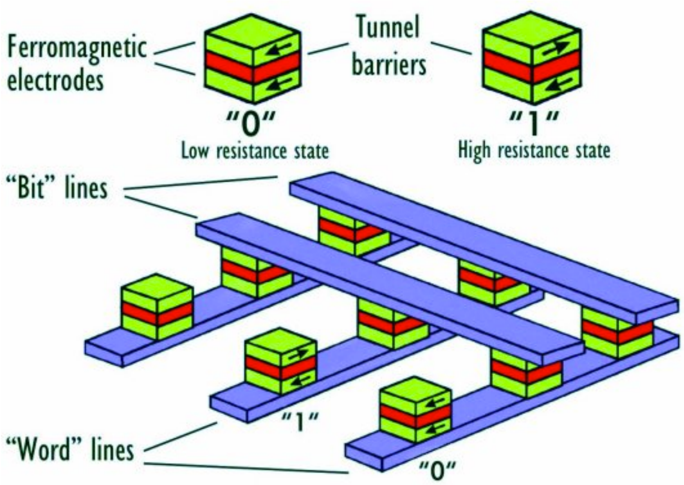

Figure 3. Magnetic random access memory spin valve. Courtesy of the National University of Singapore

These technologies (both of which offer improvements on current memory technologies) can be improved with the inclusion of PMA materials. By looking at the compositional and magnetic properties of CoCrPt as well as the magnetic, topographical, and crystallographic effects of varying the thickness of both the CoCrPt film and the Ti underlayer, a better understanding of how the magnetic properties change under various conditions.

MAGNETIC ANISOTROPY

Because the directionality of a magnetic moment is dependent on several factors, the anisotropy can be thought of as a balancing act between different properties/characteristics of the material. In the case of thin-film CoCrPt, the main contributions to anisotropy come from the shape of the material (thin film) and the crystalline anisotropy (hexagonal close packed crystal structure).

Shape anisotropy occurs because the magnetic moments preferentially align to minimize the amount of stray fields created by free poles on the surface of the magnet. These free poles in turn create a demagnetizing field, defined as:

$$H_d = -NM \tag{1}$$

Where N is the demagnetizing factor and is dependent on the shape of the material and *M* is the magnetization and is usually expressed (along with *N*, H_d) as a tensor. For a thin film (ignoring edge effects), the demagnetizing factor can be simplified as:

$$N = \begin{pmatrix} 0 & 0 & 0 \\ 0 & 0 & 0 \\ 0 & 0 & 1 \end{pmatrix} \tag{2}$$

and consequently the energy of the stray fields (E_{str}) due to the shape will be:

$$E_{str} = {}^{1}\!/_{2}\, \mu_0 M^2 \cos^2 \theta \tag{3}$$

Which gives a minimum energy of stray fields occurring at θ = 90°, indicating that an in-plane magnetization would be favorable.

Crystal structure also defines easy and hard axes within a material. An easy or hard axis is used to describe the natural alignment of the magnetic moment due to the position of the atoms. The equilibrium direction of a magnetic moment will point in the direction that minimizes the energy. For example, in some body-centered cubic (bcc) materials (like iron), it takes a significantly smaller applied field to magnetize the material along the <100> directions (an easy axis) than along the hardest directions, <111> (a hard axis). If there is no magnetic field present, the magnetic moment will be aligned in the easy direction. Similar phenomenon can be seen in materials with a hexagonal close packed (hcp) crystal structure. For example, in cobalt, the easy axis is along the [0001], [000$\bar{1}$] directions with a large field required to magnetize the material along hard axis, the basal plane, defined as the other <1000> directions. In cobalt, as is shown in Figure 4, saturation magnetization for the hard axis, [1000], exceeds 8000 Oe while the easy axis saturates at a much lower field.

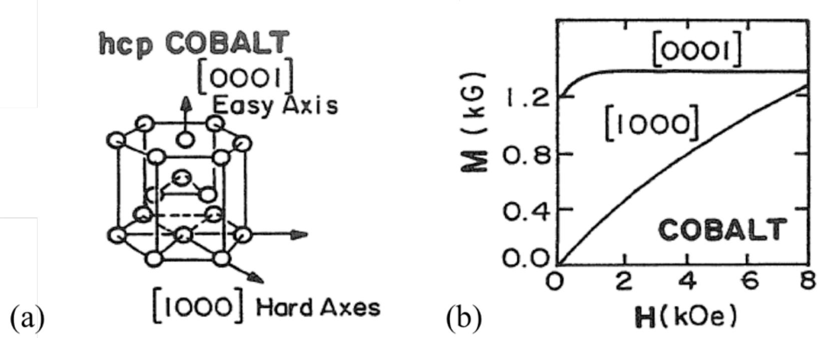

Figure 4. Crystallographic and magnetic properties of cobalt. (a) Hexagonal close packed crystal structure of cobalt with annotated easy and hard axis; (b) reaction of the magnetization of cobalt to an applied field along the hard and easy axis. Courtesy of *Modern Magnetic Materials.*[1]

Cobalt, and other materials that have a single preferential direction as their easy axis, are often referred to as uniaxial materials. The energy associated with aligning along that easy axis is defined as uniaxial crystal anisotropy energy density, which is usually expressed as a power series, though it is usually simplified to the first three terms as follows:

$$u_a = K_{u0} + K_{u1}\sin^2\theta + K_{u2}\sin^4\theta \tag{4}$$

Because K_{u0} is independent of direction, it is not helpful in understanding the anisotropy of a sample. Values for the uniaxial crystal anisotropy energy density of cobalt are reported as $K_{u1} = 4.1 \times 10^6$ erg/cc and $K_{u2} = 1.5 \times 10^6$ erg/cc[1]. A positive K_{u1} indicates a favorable z-axis orientation, as would be expected given the hexagonal packing of cobalt.

So, although shape anisotropy would dictate that thin films of CoCrPt should have an in-plane magnetization, perpendicular magnetic anisotropy (PMA) can be achieved if the magnetocrystalline anisotropy is greater than the shape determined anisotropy. By seeding the appropriate orientation of the hexagonal close packed structure of CoCrPt, an out-of-plane magnetization should dominate despite contributions from the shape.

When interfaces are present, magnetoelastic anisotropy can also affect the final directionality and magnitude of the magnetic moment. In multilayer systems, mismatch between the lattice constants and therefore the size of the unit cells will introduce strain into the lattice itself. This strain distorts the unit cell thereby changing the crystallographic and magnetic properties. For example, in a cubic system with several easy axes, applied strain can create a uniaxial system.[1]

PERPENDICULAR MAGNETIC ANISOTROPY

Perpendicular magnetic anisotropy (PMA) is a thin-film phenomenon where the shape anisotropy of the thin film is overcome, resulting in a magnetization out of the plane of the film. Shape anisotropy can be overcome by a strong crystalline anisotropy (Co alloys) or by interfaces (Co/Pt multilayers, ordered FePt intermetallic). A high PMA value is useful and sought after because it allows for higher density recording as well as increased efficiency in spin torque switching.

PMA has units of energy density, usually J/cm^3 or erg/cc. Values of PMA vary between samples and are dependent on fabrication methods as well as treatment after fabrication. However some reported values are 6.9×10^5, 3.2×10^5 erg/cc[2] for CoCr films, 3.4×10^6 erg/cc for CoCrPt films on an Cr-Ti underlayer[3], and 3.7×10^6 erg/cc for $Co_{73}Cr_{15}Pt_{12}$.[4]

As was mentioned before, a perpendicular magnetic moment requires a strong magnetocrystalline anisotropy to overcome the shape anisotropy. This can be optimized in several ways. First, the relative compositions of the elements can be tuned to maximize the out-of-plane magnetization. Second, post-deposition annealing can be used to facilitate homogenization of the films. Third, an underlayer can be added to facilitate the growth of the correct phase and crystallographic orientation of the material.

Perpendicular alignment of magnetic moments is a useful characteristic for recording high-density information. Perpendicular mediums can have a higher areal density of bits than longitudinal medium (magnetized in the plane of the film) because the tendency towards demagnetization is lower as it is stabilized against superparamagnetism.[1] Therefore, a perpendicular medium is of interest for increasing the bit-density for data storage.

COBALT CHROMIUM PLATINUM THIN FILMS

Cobalt, as was mentioned above, has a hexagonal close packed (hcp) lattice structure, leading to a magnetocrystalline anisotropy aligned on the z-axis. The energy density (see Equation 4) of cobalt is approximately $K_{u1} = 4.1 \times 10^6$ emu/cc at room temperature.[1] The lattice constants for cobalt are $a = b = 2.5071$ Å and $c = 4.0695$ Å.[5] However, these characteristics can be manipulated by alloying cobalt with other elements, allowing it to be engineered for memory storage applications.

The use of a magnetic film in memory storage devices (i.e. hard disk drives, MRAM, racetrack memory) poses an interesting engineering problem because the materials used must meet a specific set of requirements. First, out-of-plane alignment of the magnetic moments (perpendicular magnetic anisotropy, PMA) is required to maximize the areal density of the information storage as well as stabilize it against demagnetization due to superparamagnetism; second, an ideal storage material has a large enough coercivity so that it is not in danger of self demagnetizing; third, it must be able to withstand extreme environments; and fourth it must have a relatively high signal to noise ratio for an easily measurable difference between the two logic states.[1]

CoCrPt, with a PMA of approximately 8×10^6 erg/cc[6], is an excellent candidate for ultrahigh density magnetic recording material because it has a strong magnetocrystalline anisotropy that can overcome the shape anisotropy of the thin film geometry[7], it has good thermal stability[8,9], and displays very high corrosion resistance.[10] CoCrPt can be engineered to optimize its functionality as a storage device.

Cobalt naturally forms a hexagonal close packed structure. As discussed above, the magnetocrystalline anisotropy of this system leads to preferential moment alignment along the z-axis. This crystalline structure is also present in Co-Pt, Co-Cr, and CoCrPt alloys.[4].

CoPt, a candidate for PMA materials, has excellent properties. The addition of Pt to the cobalt lattice results in a small decrease in magnetization saturation[4] and the coercivity of the system is approximately 4300 Oe. It has a curie temperature of about 550 ºC and good corrosion resistance. However, the coercivity is too high for it to be used with current memory storage systems that have a limit of approximately 3000 Oe.[1] CoCr also exhibits perpendicular magnetic anisotropy. The addition of Cr to Co results in a segregation of Cr in the grain boundaries of the system. This segregation results in an increased coercivity for the system as well as a decreased saturation magnetization due to the uncoupling of the grains. However, the degree of segregation is dependent on the deposition conditions, notably temperature. The addition of other elements to Co-Cr systems has been shown to change various characteristics. Elements explored as additions to CoCr films include Pt, Nb, Ta, Zr, V, Mo, Mn, Pd, B, and Re.[11–15] However, platinum has been shown to result in the best overall properties of the films—resulting in the greatest increase in anisotropy and lowest decrease in magnetization saturization. The addition of 12-18% Pt, while decreasing the saturation magnetization slightly (by about 100 emu/cc), increases the anisotropy field from about 5 to 9 kOe.[11] CoCrPt, of varying compositions, therefore, offers an optimization of the properties present in Co-Cr and Co-Pt alloys. And, while Cr segregates to the grain boundaries, Pt is soluble into the hcp cobalt lattice, resulting in a small change in lattice parameter compared to that of a pure cobalt lattice.[16] This change is dependent on the relative composition of the Pt, but some reported values include $a = b = 2.55\text{-}2.57$Å for Pt = 10 at-%[17]

and c = 4.272 Å for Pt = 23 at-%[16]. Notably, the addition of Pt increases the perpendicular component of the system.

Underlayers can be used to control the crystallographic orientation of the magnetic film as well as the characteristics of the grains (including size, shape, and separation).[18] Specifically, in CoCrPt, the underlayer is used to induce epitaxial growth with a hcp (0002) orientation perpendicular to the film. Underlayers reported include Ti (50 nm)[19], $CrTi_{15}$ (50, 100nm)[8], Cr (150 nm)[20], Ag (20 nm)[21], NiAl (100 nm)[18], and Ta-Ru (10nm).[17] Ti naturally inspires the (0001) hcp texture in CoCrPt and has been shown to reduce the c-axis dispersion, leading to better properties.[19] There is a small lattice mismatch between Ti (a = 2.95 Å)[19] and CoCrPt (as above, a = 2.55-2.57), which introduce strain into the film at the interface between the two films. Despite this, Ti is an excellent candidate as an underlayer for CoCrPt PMA thin films.

Some studies have been done on the effects of using a Ti underlayer in a CoCrPt system. Sonobe, Ikada, Uchida, and Toyooka investigated the effects of a 25nm Ti underlayer on $Co_{72}Cr_{28}$ film (sputtered at 200 ºC) focusing on the read/write characteristics of Co-Cr.[22] Lee et al. looked at how a CoZr seed layer affected the PMA properties of $CoCr_{16.9}Pt_{10.8}$/Ti (sputtered at 240 ºC) with a focus on minimizing the thickness of the Ti layer without losing the out-of-plane magnetization.[23] Gong et al. also studied Ti as an underlayer but with an Ag seed layer for $Co_{68}Cr_{20}Pt_{12}$ (sputtered at 250 ºC) to reduce c-axis dispersion and increase out-of-plane magnetization of the sample.[19] Sun et al. performed a series of investigations on CoCrPt/Ti/NiP with NiP serving as a seed layer. Sputtering of Ti and $Co_{74}Cr_{16}Pt_{10}$ was performed at 300 ºC.[24–27] But, no work has been done for room temperature sputtering of Ti underlayers and CoCrPt films without a seed layer. This project seeks to provide insight into the relationship between the thickness of the Ti underlayer and the characteristics of CoCrPt film. Additionally, the effect of the thickness of the CoCrPt layer on the properties of the system will also be addressed. Furthermore, these results could engender studies involving the growth of PMA materials on multiferroic substrates (specifically $BiFeO_3$). CoCrPt is an excellent candidate for memory storage applications and its optimization will lead to the enabling of new technologies.

OBJECTIVES

1. Calculate the composition and Curie temperature of sputtered CoCrPt
2. Investigate the effects of changing the Ti underlayer thickness on the magnetic properties, crystallographic texture, and topography of CoCrPt thin films
3. Investigate the effects of varying the thickness of CoCrPt magnetic films on the magnetic properties, crystallographic texture, and topography of CoCrPt thin films with a constant thickness underlayer

EXPERIMENTAL DESIGN AND METHODS

Various samples were created in order to investigate the inherent properties of CoCrPt as well as to understand how varying certain parameters leads to a change in the magnetic, topographical and crystallographic characteristics of the material.

SAMPLE PREPARATION

The CoCrPt and Ti thin films were deposited at room temperature on a naturally oxidized silicon substrate (approximately 1 cm x 1 cm) by DC magnetron sputtering. $Co_{66}Cr_{22}Pt_{12}$ and Ti targets were bombarded with argon atoms, resulting in a thin film deposition on the substrate. All depositions for CoCrPt occurred at 2.1-2.3 mTorr; all depositions for Ti occurred at 8.0-8.1 mTorr. All samples were rotated at a rate of 30 min^{-1}.

To calibrate the deposition rate for both CoCrPt and Ti, silicon substrates were prepared with sharpie markings. These samples were then exposed to either Ti or CoCrPt at various powers (P = 50, 100, 150 W) for a set amount of time (t = 10, 15 minutes). The marker and film deposited on top of the marked areas were then removed using acetone. The height difference between the deposited film and the silicon substrate was measured using AFM. Nanoscope V530r3Sr3 software was used to calculate the difference between the two most common depths, giving the depth as a function of the average height of the film and the average height of the silicon substrate over an area of 1 μm x 1 μm. Several of these measurements were taken on different regions of each sample and then averaged to get an estimate of the rate. The deposition rates were as follows:

Table 1. Measured deposition rates calculated from data obtained with AFM and Nanoscope V530r3Sr3. Linear fit for deposition rate as a function of power are presented.

Titanium		$Co_{66}Cr_{22}Pt_{12}$	
Power (W)	*Measured deposition rate (nm/min)*	*Power (W)*	*Measured deposition rate (nm/min)*
50	3.5 ± 0.4	50	3.4 ± 0.1
100	6.5 ± 0.7	100	6.0 ± 0.2
150	11.1 ± 0.7	150	9.4 ± 0.4
$y = 0.074x + 0.32;\ r^2 = 0.98$		$y = 0.056x + 0.60;\ r^2 = 0.99$	

Using the linear fit obtained from the deposition rates measured on the calibration samples, regimes for the fabrication of multilayer samples were created and carried out. Samples of the following varying thicknesses were created. All CoCrPt deposition occurred at a power of 100 W. All Ti deposition occurred at a power of 50 W. In this study, the effect of varying the Ti underlayer thickness and the effect of varying the CoCrPt layer were tested, so the presentation of the samples in Table 2 reflects that goal.

Table 2. Samples prepared using dc magnetron sputtering.

Varying Ti thickness		Varying CoCrPt thickness	
Ti thickness (nm)	*CoCrPt thickness (nm)*	*Ti thickness (nm)*	*CoCrPt thickness (nm)*
20	90	80	50
40	90	80	75
60	90	80	100
70	90	80	125
80	90	80	150
90	90		
100	90		

These samples were tested to investigate their magnetic, topographical, and crystallographic characteristics. The associated error for all samples created is due to the uncertainty of the total volume of the film. The error for deposition can be summarized as ± 5nm and the Si substrate size error can be assumed to be less than 0.04 cm^2 for each sample.

SAMPLE ANALYSIS

As was described above in the Experimental Design, several characteristic techniques were used to investigate the properties of the samples created (see Table 2).

ENERGY-DISPERSIVE X-RAY SPECTROMETER

Energy-dispersive x-ray spectroscopy (EDS or EDX), usually coupled with a scanning electron microscope (SEM), can be used to investigate the composition of a sample. EDS uses an electron beam to excite the material; when the incident electron causes the dislodging of an inner electron, an electron from one of the outer orbitals will fall to a lower energy state to replace it. This change in energy level releases an x-ray with a wavelength characteristic to the elemental identity of the atom. The x-rays emitted from a sample are detected and used to identify the overall elemental composition of the sample. In general, the results are given as a set of peaks, with the axes being energy (usually units of keV) versus intensity (usually units of cts or au). By comparing the area under these peaks, the relative composition can be calculated.

All EDS results were obtained using a JEOL 6610LV SEM with Iridium Ultra EDS software used for calculations of composition. All samples were cleaned using compressed air and mounted on standard SEM stubs to ensure a level testing surface. All results were taken in high vacuum. At least three measurements were taken from different regions of the sample.

VIBRATING SAMPLE MAGNETOMETER

A vibrating sample magnetometer creates a uniform magnetic field in which a sample is vibrated. Coils, placed near the sample, pick up the voltage induced by the moving sample (see Figure 5). This voltage is proportional to the magnetic moment of the sample at that applied field.

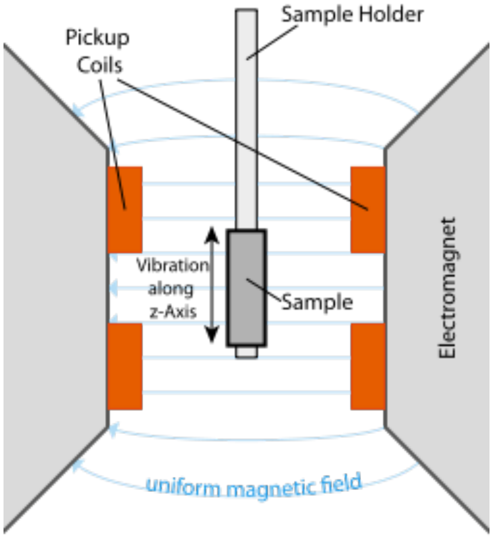

Figure 5. Schematic of a vibrating sample magnetometer. Courtesy of Wikipedia.

In a standard experiment, the field is set at -10,000 Oe and is incrementally changed until it reaches 10,000 Oe. The regime is then reversed and measurements are taken as the field decreases back to it’s original value. The hysteresis loops obtained from this measurement can be used to calculate the saturation magnetization, coercivity, remanence, squareness, switching field distribution (SFD), and anisotropy energy density of a sample. A hysteresis loop has an x-axis of applied field, *H* (Oe), and a y-axis of magnetization, *M* (emu/cc) (see Figure 6).

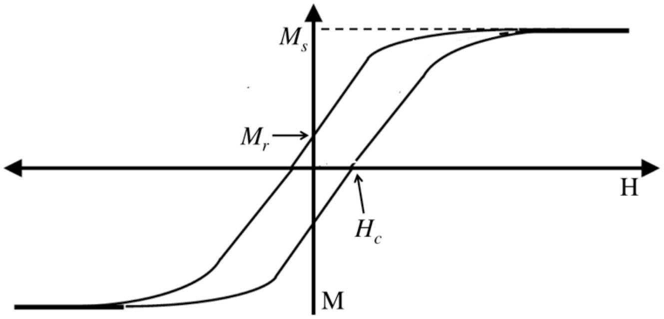

Figure 6. Standard hysteresis loop for a magnetic material. M_s denotes the saturation magnetization, H_c the coercivity, and M_r the remanence.

The saturation magnetization, M_s (emu/cc), is the magnetization of the material at saturation, or the maximum magnetization possible for a sample. This value should be an inherent materials property because it is in effect a measure of the strength and density of the magnetic moments contributed by each atom. However, in some cases, the sample will not saturate at the maximum applied field. In this case, a superconducting quantum interference device (SQUID) or another instrument that can achieve higher values of field should be used to calculate the magnetization saturation.

The coercivity, H_c (Oe), of a sample is the applied field required to achieve a sample with zero net magnetization. The coercivity of a sample should be independent of the directionality of the test; if it is not, the sample is said to have an exchange bias. The remanent magnetization or remanence, M_r (emu/cc), is the magnetization of the sample when the applied field equals zero after being saturated. The squareness of a sample is given as the ratio of the remanence to the saturation magnetization; see the equation below:

$$S = \frac{M_r}{M_s} \tag{5}$$

Squareness is useful as a comparative tool and is a representation of the strength of the readable signal in the absence of a field ($H = 0$). A higher squareness is desirable for recording media.

The anisotropy energy density, K_{u1} is discussed theoretically above. Experimentally, the value K_{u1} can be calculated as either

$$K_{u1} = \frac{1}{2} M_s H_k \tag{6}$$

Where M_s is the saturation magnetization of the easy axis loop and H_k is the anisotropy field, equal to the field where the easy axis and hard axis loops intercept. This method for calculating the anisotropy energy density is flawed because, for hard axis loops (in this case, in-plane), the corrected data often is approximated to have a magnetization saturation that is lower than that of the easy axis. Because this data has been corrected, the anisotropy field (H_k) is difficult to approximate. Another method (and the method that will be used in this project) for finding the value of the anisotropy energy density is to find the difference in area between the easy and hard axis loops in the first quadrant of a standard hysteresis loop ($H > 0$; $M > 0$).[1] Because it is a measure of the difference in the amount of energy it would take to align the magnetization along the easy axis versus the hard axis, a high anisotropy energy density is desirable to prevent demagnetization and to increase thermal stability.

The switching field distribution (SFD) can be calculated by finding the full width, half maximum (FWHM) of the Gaussian fit of the derivative of the *M-H* curve plotted against the applied field (H) values. In this project, the form of the Gaussian fit was as follows:

$$f(x) = a \exp\left[-\left(\frac{x-b}{c}\right)^2\right] \tag{7}$$

The SFD is a measure of the size distribution of particles, with a high SFD correlating to more homogenous distribution of sizes. For use in magnetic storage, regular grains are desirable as irregular grain shapes lead to noise when reading the data.

The Curie temperature can also be found by taking measurements at different temperatures. The Curie temperature is defined as the temperature at which the saturation magnetization approaches zero and the hysteresis loops show a paramagnetic response.

The VSM used for all experiments presented here was a DMS Model 1600 Signal Processor, Model 32KG Gaussmeter, Model 883A Temperature Controller as well as MicroSense VSM. The data was recorded using the MicroSense EasyVSM program.

For each sample, the recipe for the VSM was as follows (ΔH indicates step size): ΔH = 500 Oe for H = [-10000, -2000], ΔH = 200 Oe for H = [-2000, 2000], ΔH = 500 Oe for H = [2000, 10000] where H is the applied field (units Oe) and the recipe is repeated in the opposite direction as well (10000 to -10000 Oe).

To test the Curie temperature, samples were held at temperature (T = 150, 250, 300, 350, 400, 450, 500, 600 ºC) for 15 minutes, then the testing as described above was completed and the sample was cooled to room temperature before another test was performed.

One major source of error in the calculating the aforementioned values (saturation magnetization, coercivity, etc.) is the uncertainty in calculating the total volume of the sample since the results are reported in emu/cc instead of emu, as is recorded by the instrument. Any errors in thickness, or in the measurements of the dimensions for the samples will be carried forward and will affect the final values presented. Additionally, the step size of the measurements can account for some of the error, with large step sizes resulting in more uncertainty.

X-RAY DIFFRACTOMETER

X-ray diffraction provides important information about the crystallographic orientation of the sample as well as the phases present. As is shown in Figure 7, the x-ray's are emitted at the source and are directed towards the sample at varying angles resulting in data that is plotted as 2θ versus intensity (cts or au).

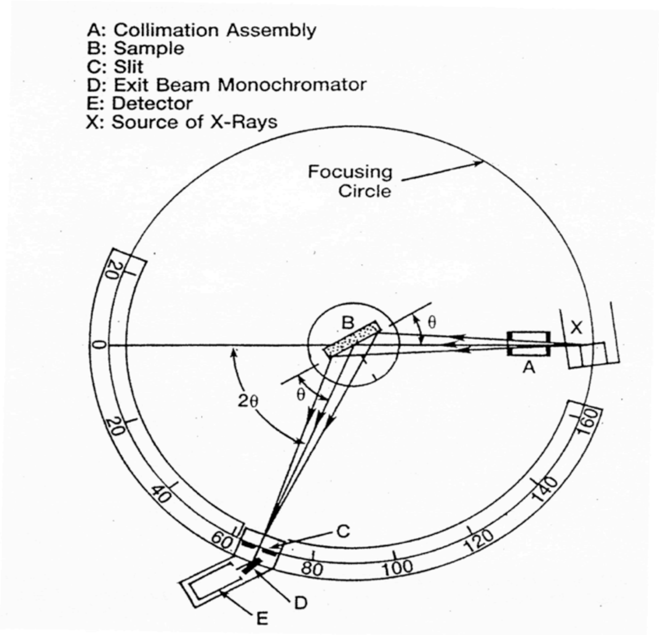

Figure 7. Schematic of an x-ray diffractometer. Courtesy of Dr. Meri Treska.

In accordance with Bragg's law (see Equation 8 below), when the corresponding plane is present in the material, the reflected x-rays will constructively interfere, resulting in peaks at a specific value of 2θ.

$$n\lambda = 2d\sin\theta \tag{8}$$

Where d is defined as the spacing between the planes, n is a positive integer, and λ is the wavelength of the radiation (for a Cu K-α source, 0.15406 nm). A value for d can be calculated using the following formula:

$$d = \frac{a}{\sqrt{h^2 + k^2 + l^2}} \tag{9}$$

where *a* is equal to the lattice constant associated with the plane and *h*, *k*, and *l* are the miller indices of the incident plane (hkl).

Though the intensity (cts) of these peaks cannot be compared between results of different samples, intensities of peaks within the same run of a sample can be compared. For example, a comparison between the intensity of the (0001) peak and the intensity of the $(10\bar{1}0)$ peak of an hcp material would result in a comparative intensity factor, *m*, as below:

$$m = \frac{I_{(0001)}}{I_{(10\bar{1}0)}} \tag{10}$$

This factor gives an idea of the alignment of the crystal and which planes are aligned to better interact with the radiation source. In hcp CoCrPt, a strong (0001) peak is desirable.

All samples were crystallographically investigated using a PANalytical X'Pert PRO XRPD. No additional preparation of samples was performed. The scans were run from 2θ = 20º - 80º with a scan step size of 0.0167º. Peaks were identified and matched using the X'Pert Highscore software database.

ATOMIC FORCE MICROSCOPE

Atomic force microscopy can be used to investigate the topography of a surface. A cantilever with a pyramidal point at the tip is linearly tapped along the surface of the material. This is done repeatedly to create an image of the surface of the sample. Changes in the response of the cantilever are measured by the reflection of a laser that is centered, at rest, on the tip of the cantilever. An atomic form microscope (AFM) allows the user to calculate the depth of an edge, the roughness of a sample, and several other functionalities. However, atomic force microscopy gives no information on the composition of the film itself and requires a specific magnetic tip to analyze magnetic domain size and structure.

All results presented were obtained with a Dimension 3100 Atomic Force Microscope (Nanscope IV SPM Control Station, Veeco) and were processed using Nanoscope V530r3Sr3 software. The sample size for each reading was 1.0 µm by 1.0 µm and the maximum scan speed for the tip was 4.0 µm/sec. At least three regions of each sample were tested and the values presented are the averages of these three regions.

RESULTS AND DISCUSSION

This project will be divided into three sections to best discuss the results of this study. The first is the composition and magnetic properties of CoCrPt, which will present the data concerning the measured composition of the samples, and the curie temperature of the CoCrPt films used in this report. Second, the effects of changing the thickness of the Ti underlayer will be discussed with respect to the topographical roughness, the crystallography, and the magnetic properties: saturation magnetization, coercivity, remanence, squareness, SFD, and anisotropy energy density. The same characterization studies were undertaken to understand the effect of varying the thickness of the CoCrPt magnetic layer.

COMPOSITION AND MAGNETIC PROPERTIES OF COCRPT

Several investigations were carried out to better understand the properties of the CoCrPt alloy fabricated. Results for both composition and Curie temperature are presented below.

COMPOSITION

The composition of the sputtered CoCrPt thin films was investigated with EDS. All samples tested had an underlayer of 80 nm Ti. The averaged composition from these samples was $Co_{60.2}Cr_{16.4}Pt_{23.4}$ (subscripts represent atomic percent measured) and the results from each sample are presented in Table 3 below:

Table 3. Composition (at-%) of CoCrPt thin films created by sputtering off a $Co_{66}Cr_{22}Pt_{12}$ target. Compositions shown are an average of at least 5 measurements at different points on the sample; error reported is the maximum standard deviation of the data for each sample

Sample Thickness (nm)	*Composition*	*Error*
75	$Co_{60.2}Cr_{16.2}Pt_{23.6}$	± 1.0%
100	$Co_{59.3}Cr_{16.1}Pt_{24.6}$	± 0.7%
125	$Co_{60.2}Cr_{16.5}Pt_{23.3}$	± 0.4%
150	$Co_{61.1}Cr_{16.7}Pt_{22.2}$	± 0.5%

This measured composition differs from the reported value on the target used, ($Co_{66}Cr_{22}Pt_{12}$) though the reported composition is very consistent between samples of different thicknesses.

This inconsistency is probably due to different sputtering rates of elements. Because each constituent has a different sputtering rate, it is difficult to maintain the same stoichiometry in the sputtered film as is found in the multicomponent target. Because several scans were done at many different points of the samples, it is unlikely that the films are macroscopically (area > 50 μm) heterogeneous. This composition has implications for the characteristics discussed below because amount of platinum added to the Co-Cr system has been shown to affect the properties of the system.

Because Pt is known to increase the stacking fault density in CoCrPt[28], a larger percentage of Pt could disrupt homogenous uniaxial grain growth. These stacking faults would lead to a weaker PMA material. In direct competition with this effect is the effect that the addition of Pt has on the magnetocrystalline anisotropy and magnetostriction. Liu et al. reported that for $(Co_{90}Cr_{10})_{1-x}Pt_x$ on a CrW underlayer an increase from $x = 8.5$ at-% to 25 at-% results in an increase in both magnetocrystalline and magnetoelastic anisotropy. These increases generally lead to an increase in coercivity and are caused by the changes in the lattice parameters of the CoCrPt samples ($a = 2.537$ to 2.617 Å; $c = 4.141$ to 4.272 Å) and the resultant change in the mismatch between the CoCrPt and the underlayer.[16] So, though the high concentration of Pt could potentially interrupt the crystallographic structure of the film, it also results in a comparatively larger magnetocrystalline anisotropy than would be expected in a film with a lower concentration of Pt.

It is also possible that this high percentage of Pt could have promoted uniaxial growth of PMA CoCrPt. A 90nm film of CoCrPt on bare naturally oxidized Silicon had the hysteresis loop shown in Figure 8.

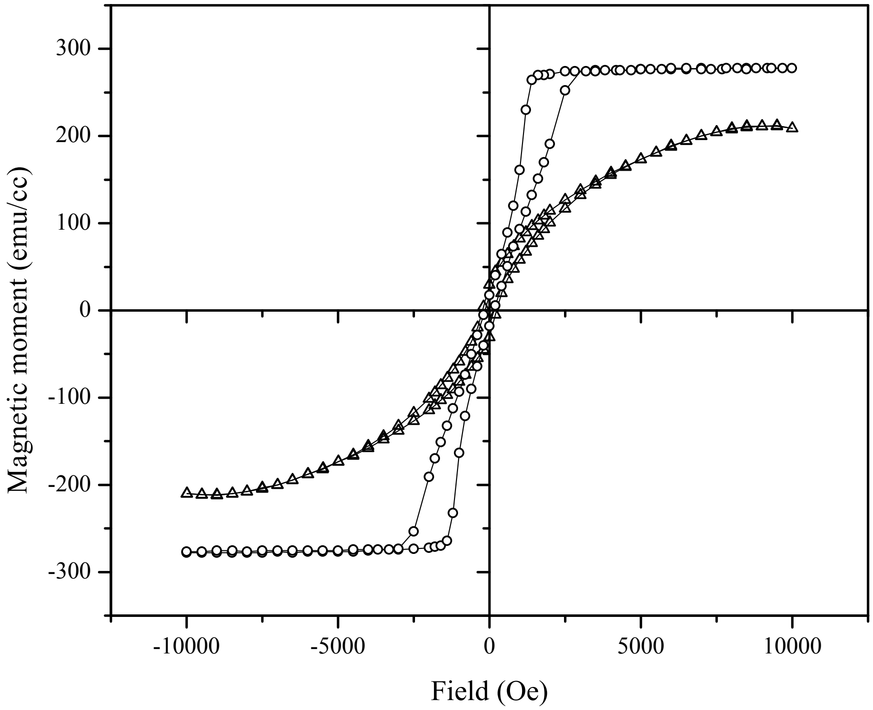

Figure 8. In-plane and out-of-plane hysteresis loops for $Co_{60.2}Cr_{16.4}Pt_{23.4}$ (t = 90nm) on bare, naturally oxidized Si. Circles (○) indicate out-of-plane directionality of testing; upward facing triangles (△) indicate in-plane directionality for testing. Lines connect points.

The in-plane hysteresis loop appears to represent the hard axis of the material, requiring a large field to saturate. The out-of plane hysteresis loop, on the other hand saturates relatively quickly, indicating an easy axis.

Because there is clear difference in the shape of the curves, there is anisotropy present in this material. In comparison with the easy and hard axis *M-H* curves in Figure 4, it follows that the out-of-plane magnetization is more energetically favorable than the in-plane magnetization (which is still not saturated at 10,000 Oe). Ergo, the CoCrPt film seems to behave like a PMA material even without an underlayer present.

CURIE TEMPERATURE

A 140nm CoCrPt film with no Ti underlayer on a naturally oxidized silicon substrate was tested to calculate the Curie temperature of the composition of the sputtered samples. The out-of-plane hysteresis loops at different temperatures are presented below in Figure 9:

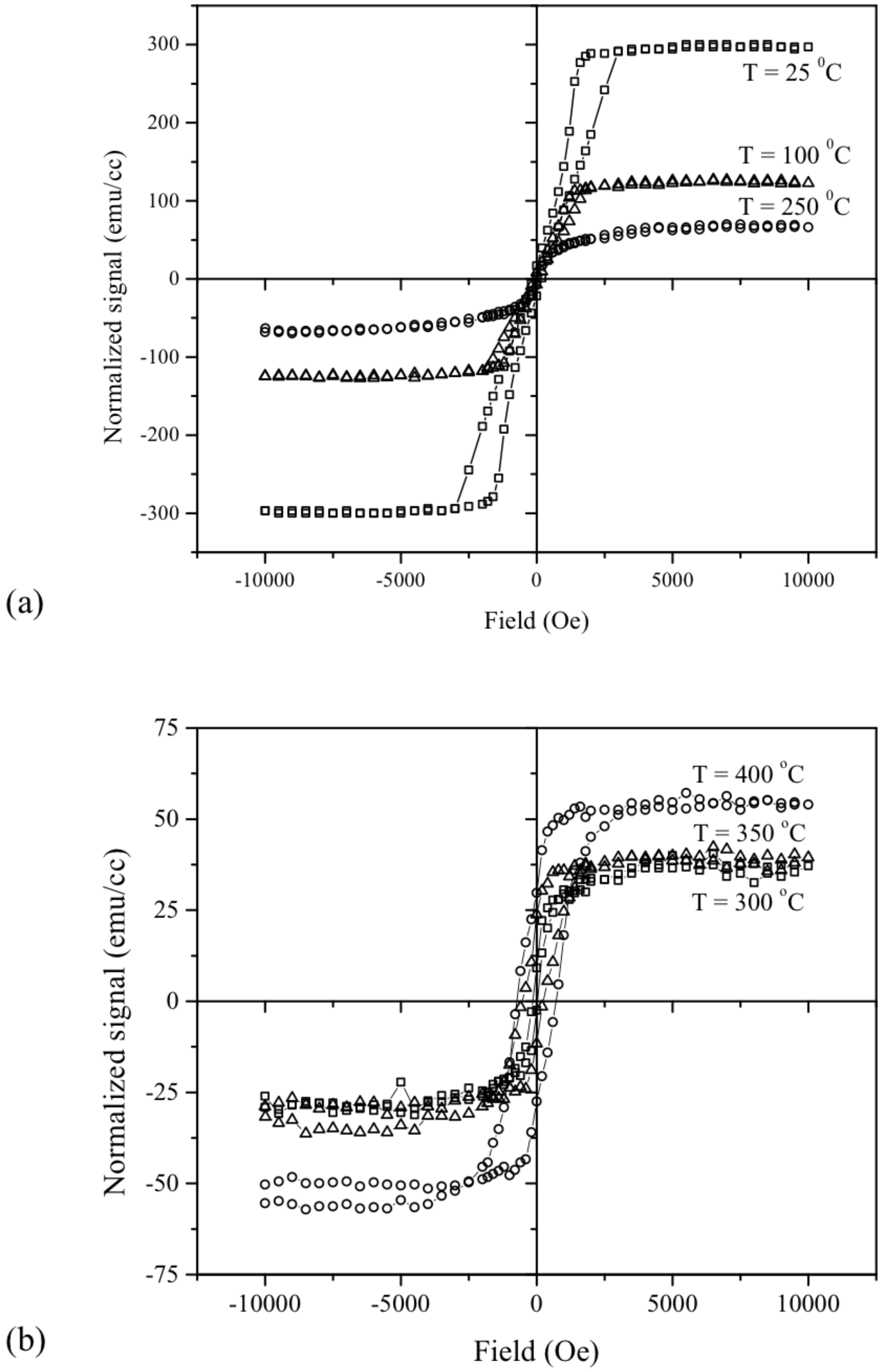

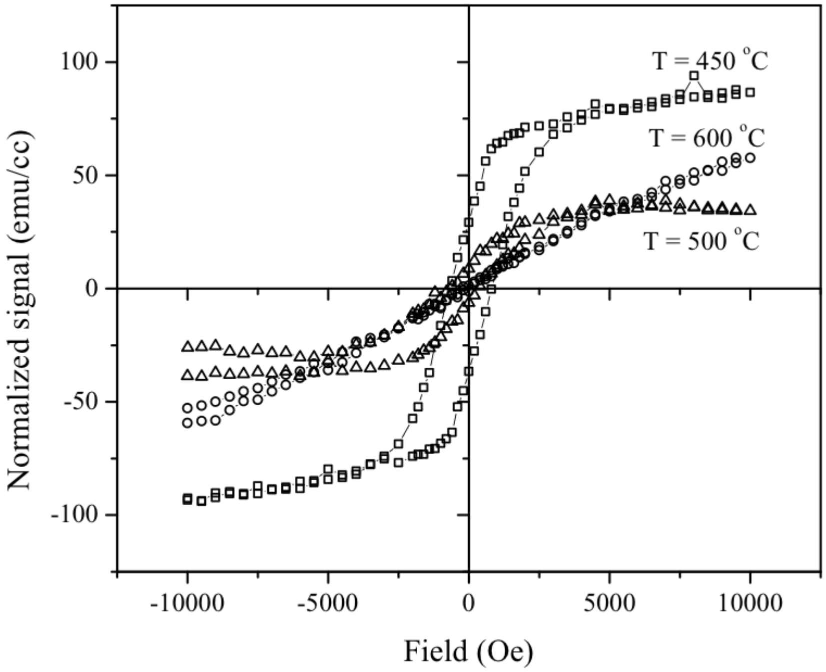

(c)

Figure 9. Out-of plane M-H curves for CoCrPt thin films (*t* = 140nm) at different temperatures, as labeled in images. For clarity, only three loops are shown for each graph; parentheses indicate the symbol used. (a) shows T = 25(□), 100(△), 250(○) ºC; (b) shows T = 300 (□), 350(△), 400(○) ºC; (c) shows T = 450(□), 500(△), 600(○) ºC. Lines connect points.

The trends in magnetization saturation, coercivity, remanence, and squareness of the temperature dependent out-of-plane hysteresis loops are reported below in Figure 9:

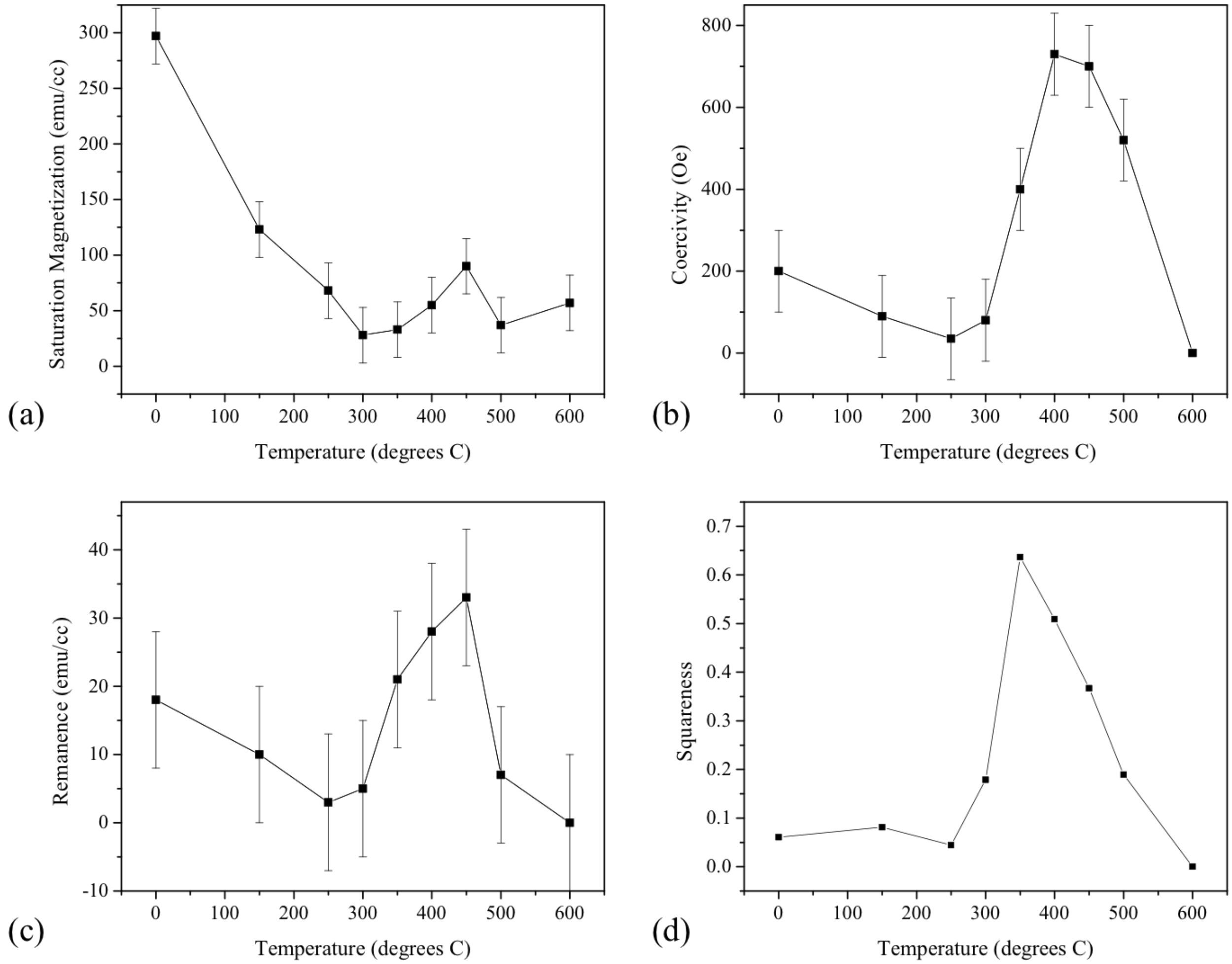

Figure 10. Magnetic properties of CoCrPt (*t* = 140nm) for different temperatures; (a) presents the saturation magnetization; (b) the coercivity; (c) the remanence; (d) the squareness. Lines connect points.

The out of plane saturation magnetization (Figure 10a) trends downwards, eventually approaching paramagnetic behavior at or before 600 ºC. The coercivity, remanence, and squareness (Figure 10b, c, d) show a different trend, with an increase starting at 300 ºC before decreasing to zero.

The magnetization saturation decreases as would be expected with increasing temperature, though it does not reach zero at 600 ºC. However, the sample appears to exhibit parametric behavior when tested at 600ºC because it has an approximately linear slope (see Figure 9).

Though, when the field is at its maximum value (H = 10,000 Oe), the magnetization value is approximately 57 Oe, not zero as one might expect. However, there is no visible hysteresis and the sample appears to be behaving paramagnetically.

The increasing then decreasing trend, displayed in coercivity, remanence, and squareness is potentially due to some annealing that occurred while the sample was held at temperature, allowing it to reorder into a structure that has better PMA characteristics. This effect was studied by Sun et al. who annealed their $Co_{74}Cr_{16}Pt_{10}$ ($t < 40$nm) at 550 ºC for 10 minutes in a vacuum furnace and reported an increase of approximately 1000 Oe in coercivity when measured at room temperature following the treatment.[27]

Another process that could be occurring is the preferential oxidization of Cr. Because Cr is the most easily oxidized in the CoCrPt sample, the amount of Cr available to participate in the magnetic properties of the sample is lower than that reported in the composition.[2] If the Cr is able to segregate in the grain boundaries, the resulting less chromium in the grain boundaries due to oxidation could explain the trends observed in coercivity, remanenece, and squareness in Figure 10.

To confirm that a physical change occurred in the samples, one sample, held at 500 ºC for approximately 40 minutes was tested at room temperature and compared to the out-of-loop hysteresis loop with no annealing in Figure 11:

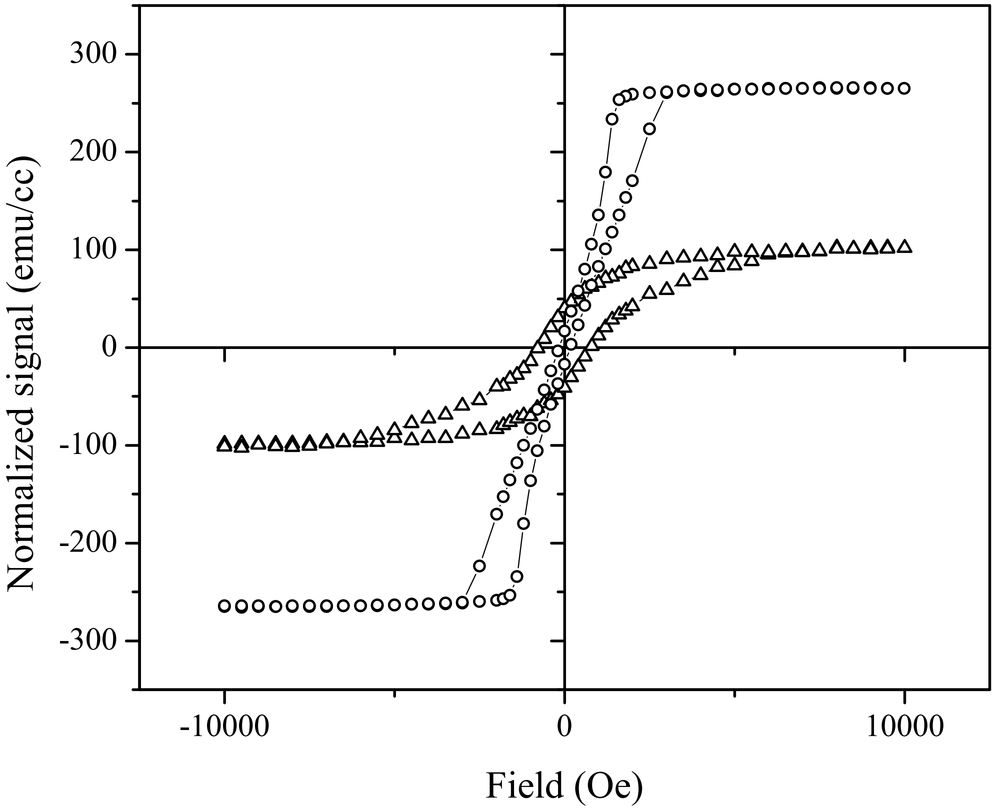

Figure 11. Out-of loop hysteresis loops for CoCrPt (*t* = 140nm) films with no post-fabrication treatment (circle ○) and annealing at 500ºC for approximately 40 minutes (upward facing triangle △). Lines connect points.

There is a notable decrease in magnetization saturation, from approximately 265 emu/cc without post fabrication processing to 100 emu/cc with the 500 ºC anneal. There is also an increase in coercivity, from 165 Oe with no annealing to 795 Oe.

These changes in magnetic properties are likely due to the segregation of Cr to the grain boundaries along with, potentially, the oxidation of this Cr. Additionally, the change in magnetic properties in Figure 11 show that in the process of measuring the Curie temperature, the films' properties change.

EFFECTS OF VARYING TI UNDERLAYER THICKNESS

The thickness of the Ti underlayer (*t* = 20, 40, 60, 70, 80, 90, 100) has a large effect on many of the properties of thin-film CoCrPt. For clarification, the results have been separated into three sections: magnetic properties, crystallography, and topography.

MAGNETIC PROPERTIES

The hysteresis loops obtained with a MicroSense VSM for samples of varying Ti thickness are presented in Figure 12 below:

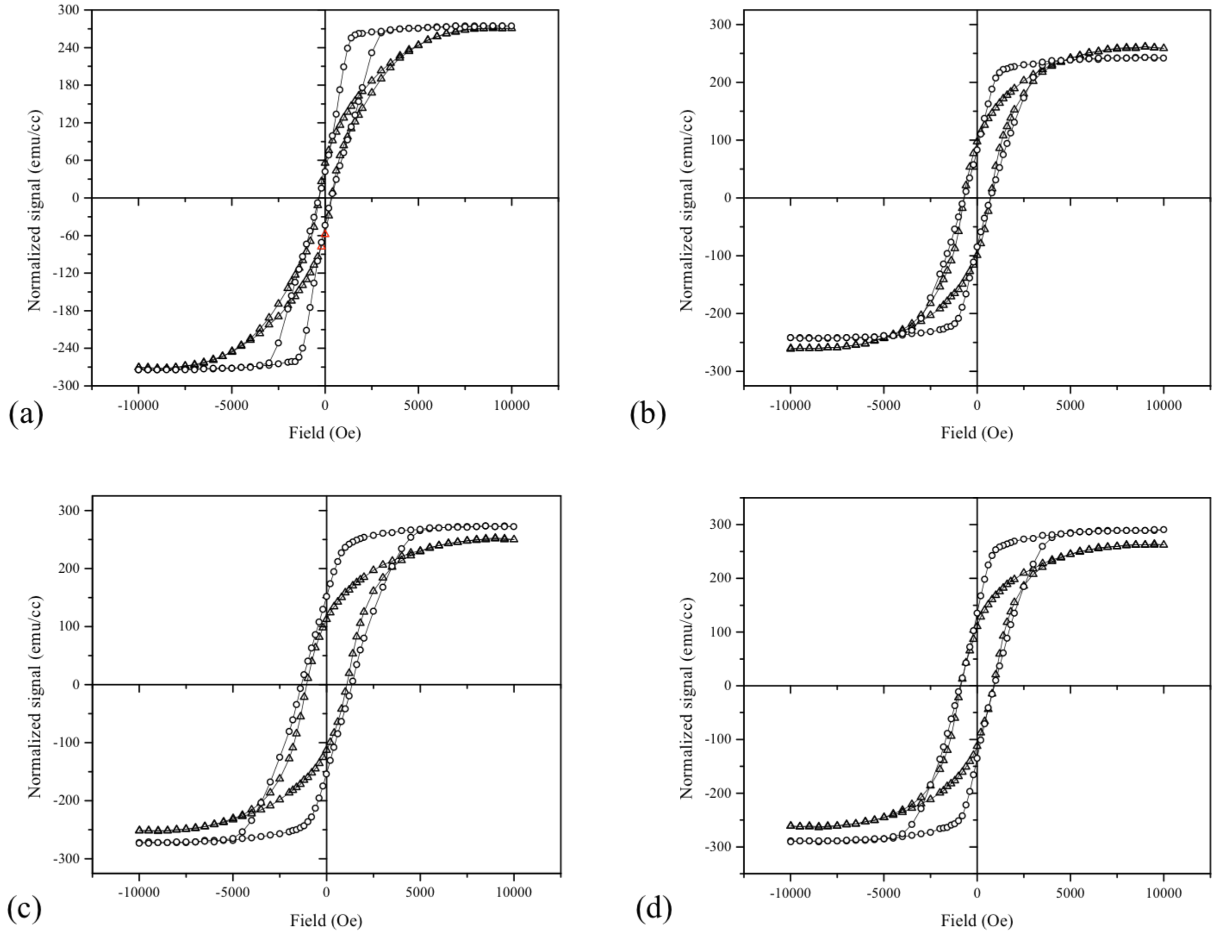

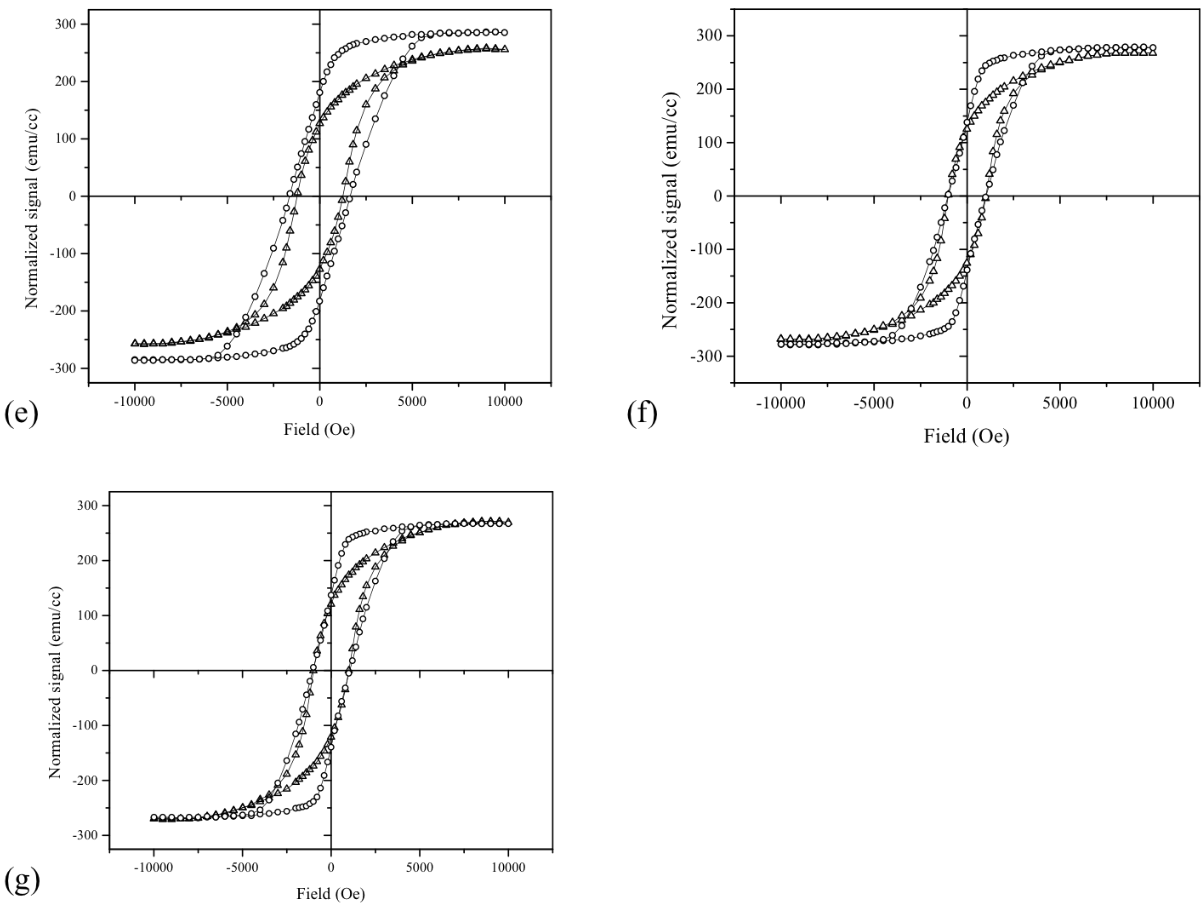

Figure 12. M-H curves for CoCrPt thin films (*t* = 90nm) with varying Ti underlayer thickness. In each graph, a circle (○) indicates out-of-plane loops and an upward facing triangle (△) indicates the in-plane loops. Underlayer thickness values are as follows (a) *t* = 20nm; (b) *t* = 40nm; (c) *t* = 60nm; (d) *t* = 70nm; (e) *t* = 80nm; (f) *t* = 90nm; (g) *t* = 100nm. Lines connect points.

The magnetic properties, specifically the magnetization saturation, coercivity, remanence, squareness, switching field distribution, and anisotropy energy density, were calculated and are presented in Figure 13 as a function of Ti underlayer thickness.

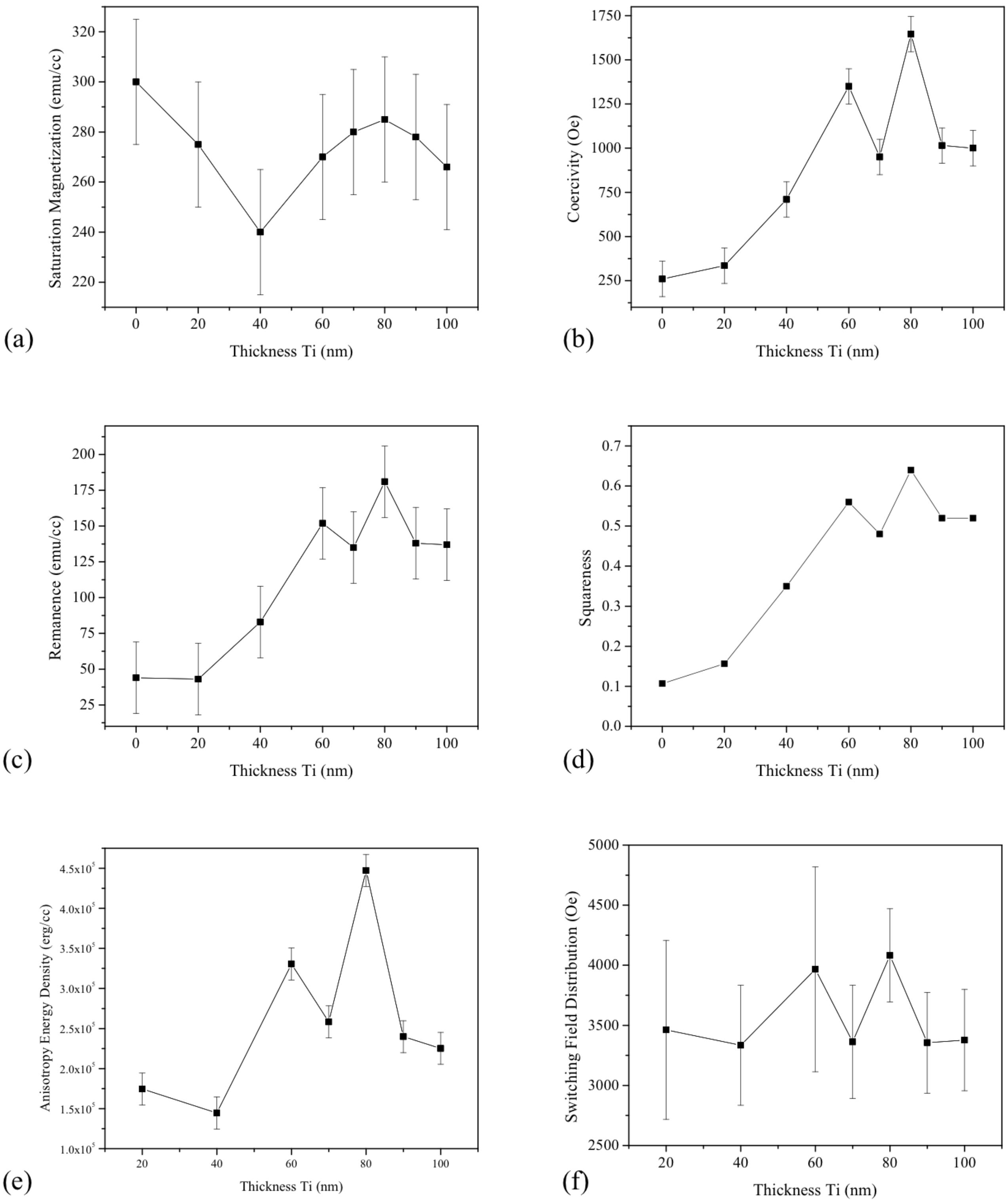

Figure 13. The out-of-plane magnetic properties of CoCrPt (*t* = 90nm) and variable Ti underlayer thickness (*t* = 20, 40, 60, 70, 80, 90, 100nm). The properties are as follows (a)

magnetization saturation (emu/cc), (b) coercivity (Oe), (c) remanence (emu/cc), (d) squareness, (e) switching field distribution (Oe), (f) anisotropy energy density (erg/cc). Lines connect points.

The saturation magnetization (Figure 13a), though changing slightly, does not show a dramatic dependence on the thickness of the underlayer. The greatest difference is a 20% decrease between $t = 0$ and $t = 40$nm. The coercivity (Figure 13b) steadily increases until it seems to stabilize above 60nm Ti at about 1200 Oe. The remanence (Figure 13c) follows a similar trend as the coercivity, showing initial increase that eventually levels off at or above 60nm Ti with a difference of about 400% between $t = 20$nm and $t = 60$nm. The shape of the squareness (Figure 13d, calculated using Equation 5) also follows the trend seen in the remanence and coercivity, with a 500% increase between $t = 20$nm and $t = 60$nm.

The anisotropy (Figure 13e) shows an increase, then a decrease in a trend very similar to those described above for coercivity, remanence, and squareness. There is an approximately 300% difference between the lowest value (at $t = 40$nm) and the highest value (at $t = 80$nm) reported. However, the switching field distribution (Figure 13f), much like the saturation magnetization, does not show a clear trend with changing underlayer. The greatest difference is between a Ti thickness of $t = 40$nm and $t = 80$nm, which shows an approximately 20% decrease.

The differences between values for magnetization saturation (i.e. between M_s of $t = 0$ and $t = 40$nm) can be explained by possible errors in calculations of volume of the film present. In general, since the composition of the material does not appear to differ greatly between samples (Table 3), the saturation magnetization should be constant, which seems to be confirmed by the data presented in Figure 13a.

The increase in coercivity as Ti thickness increases implies that at around 60nm, the texture of the Ti is sufficient to nucleate substantial (0002) growth in the CoCrPt film. This increased grain growth and organization would lead to a higher coercivity because columnar grains forming in the c-axis direction, (0002), would allow for a macroscopic out-of-plane orientation of magnetic moments. The growth of columnar grains requires a certain threshold thickness, which according to the data in Figure 13b is at approximately $t = 60$nm. This columnar grain growth, along with the fact that chromium (with an at-% lower than 18) segregates at the grain boundaries, isolating the grains and allowing for a greater coercivity[1], explains why there is an observable increase in coercivity

The increase in remanence is similarly motivated because the factors that increase coercivity should also increase the remanent magnetization (at zero applied field). An increase in remanence means that there is a stronger preference for an out-of-plane easy axis orientation of the magnetization. The uniaxial growth of hcp CoCrPt due to columnar grains of Ti increases the favorability of magnetization to point out-of-plane. The trend in the squareness, very similar to both the trend in remanence and the coercivity, is dominated by the remanence (found in the denominator of Equation 5) since there is no dramatic change in magnetization saturation as Ti thickness changes.

The anisotropy, which shows a similar trend to coercivity, remanence, and squareness, is also a reflection of how strongly aligned out of plane the magnetization. As a measurement of the difference in the amount of energy it would take to align the magnetic moment along the easy and hard axis, the increase in anisotropy energy density can be understood as an indication that it is more favorable for the moments to align perpendicular to the plane (c-axis).

Any differences SFD between the different thicknesses can be explained first by errors in calculating the volume of the sample and secondly by the inaccuracy of the Gaussian fits (Equation 7) used to calculate the SFD. The fits used to calculate the values presented in Figure 13f are given below in Table 4.

Table 4. Gaussian fits used to calculate the switching field distribution of samples with varying Ti underlayer thicknesses. See Equation 7.

Ti underlayer thickness (nm)	*A*	*b*	*c*	*R^2 value*
20	0.15	217.7	2076	0.84
40	0.13	557.8	2002	0.92
60	0.13	1279	2382	0.96
70	0.15	808.4	1974	0.93
80	0.12	1595	2626	0.96
90	0.15	907.2	2015	0.94
100	0.14	942.5	2028	0.94

Most of the R^2 values are greater than 0.90, indicating a fairly good fit for the data. However, some of the variation in the reported SFD (full width half maximum value) could be explained by this factor.

CRYSTALLOGRAPHY

The texture of the samples was interrogated using a PANalytical X'Pert PRO XRPD X-ray diffractometer. Figure 14 presents the superimposed data from several samples with different underlayer thickness.

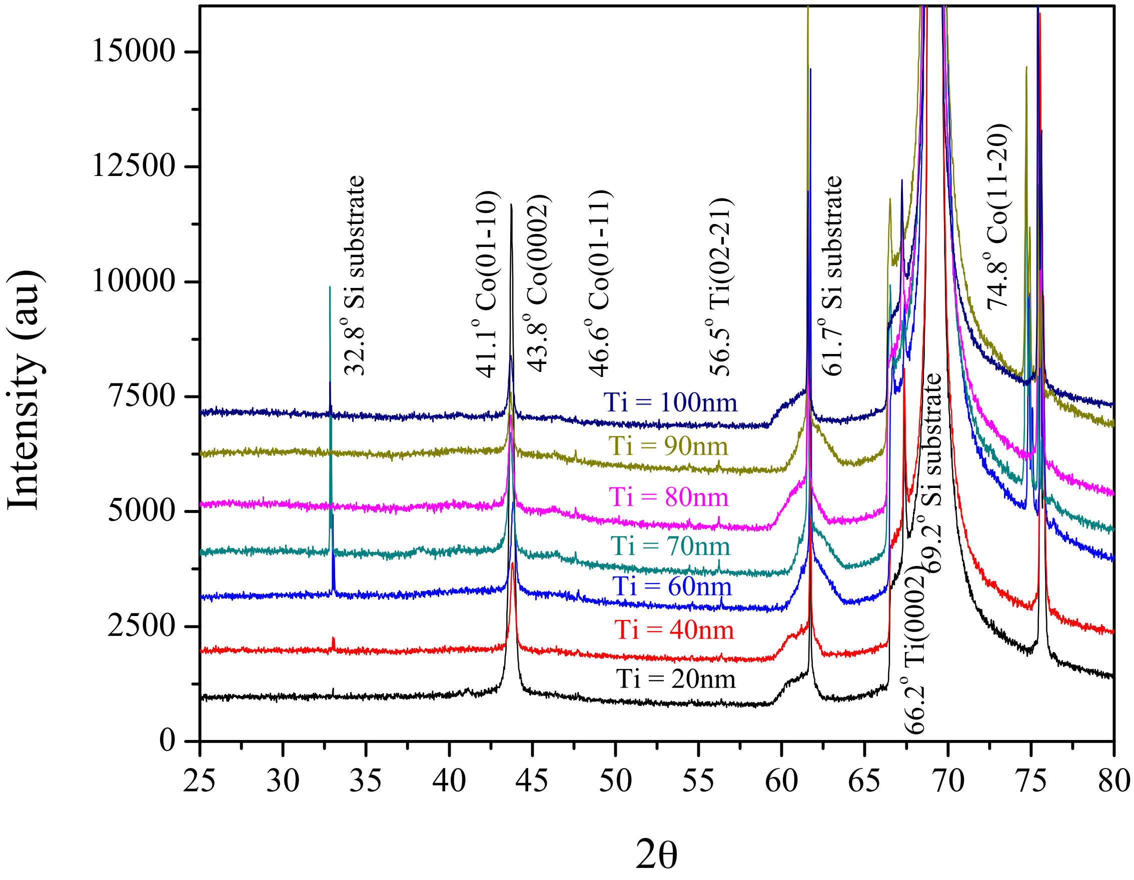

Figure 14. XRD scans for 90nm CoCrPt films with varying Ti underlayer thickness (*t* = 20, 40, 60, 70, 80, 90, 100nm). Peaks identified using X'Pert Highscore software databases.

The peaks present in any of the samples presented are labeled in the above figure. The identification of these peaks was achieved with X'Pert Highscore software. All samples showed evidence of the (0002) plane, though with increasing underlayer thickness, the (0002) peaks shift left. All substrate and titanium peaks do not appear to shift with changing underlayer thickness.

All CoCrPt samples indicate the presence of the (0002) plane. Other planes that are present include $(01\bar{1}0)$ at *t* = 20nm and $(01\bar{1}1)$ at *t* = 70, 90, 100nm though the intensity of these peaks is very low compared to the (0002) plane. Both planes never achieve more than 10% of the intensity of the c-axis (0002) plane. The $(11\bar{2}0)$ plane has a strong presence in the samples where *t* = 60 and 70nm. Table 5 presents the relevant information for the (0002) peak identities for all samples.

Table 5. Crystallographic values acquired with XRD scans (step size 0.0167º) for varying Ti underlayer thickness (*t* = 20, 40, 60, 70, 80, 90, 100nm). Values calculated with X'Pert Highscore software.

Ti thickness	*(0002) peak location (2θ)*	*d* (Å)	*c* (Å)	*FWHM*
20	43.72	2.071 ± 0.002	4.142 ± 0.002	0.4512 ± 0.008
40	43.80	2.067 ± 0.002	4.134 ± 0.002	0.2342 ± 0.008
60	43.84	2.065 ± 0.002	4.130 ± 0.002	0.2342 ± 0.008
70	43.68	2.072 ± 0.002	4.144 ± 0.002	0.2342 ± 0.008
80	43.70	2.071 ± 0.002	4.142 ± 0.002	0.2342 ± 0.008
90	43.69	2.072 ± 0.002	4.144 ± 0.002	0.2342 ± 0.008
100	43.69	2.072 ± 0.002	4.144 ± 0.002	0.2007 ± 0.008

The shifting of the (0002) peak results to lower peak in a larger *c* lattice constant (see Figure 4 [0001] easy axis for reference). The *d* value (calculated using Equation 8) is directly dependent on the peak location and *c*; the lattice constant can be derived from the plane spacing, *d* (see Equation 9). The full width, half maximum values remain constant except for *t* = 20nm which features a much wider peak and *t* = 100nm which features a slightly skinnier peak.

Since the unit cell volume is kept constant, this increase in the *c* lattice constant would lead to a decrease in the *a* lattice constant. This elongation of the lattice cell would theoretically increase the magnetocrystalline energy, and so increase the anisotropy. This increase in anisotropy energy density with increasing Ti thickness is supported by the data reported in Figure 13e. This trend implies that better PMA materials are created at higher thickness of Ti underlayer.

The FWHM values should give an insight into the c-axis dispersion, or how broad the distribution of orientations of each moment is. Because the FWHM values are constant for most of the values, it can be assumed that except for edge cases, the underlayer thickness does not greatly affect the c-axis dispersion of a sample. However, as will be discussed in the Conclusion, there are other methods to more accurately test this value that could help distinguish if there is any change due to Ti underlayer thickness. However, at t = 20nm, the FWHM is nearly twice the value of the other samples. This implies that the film was more disordered with less homogenous uniaxial growth, probably because the Ti film was too thin to allow for sufficient influence on the CoCrPt films.

TOPOGRAPHY

The roughness of the samples shows a trend of increasing roughness as thickness of the CoCrPt layer increases. As is shown in Figure 15, the 80nm Ti underlayer sample has an approximately four times rougher surface than the sample with a 20nm underlayer.

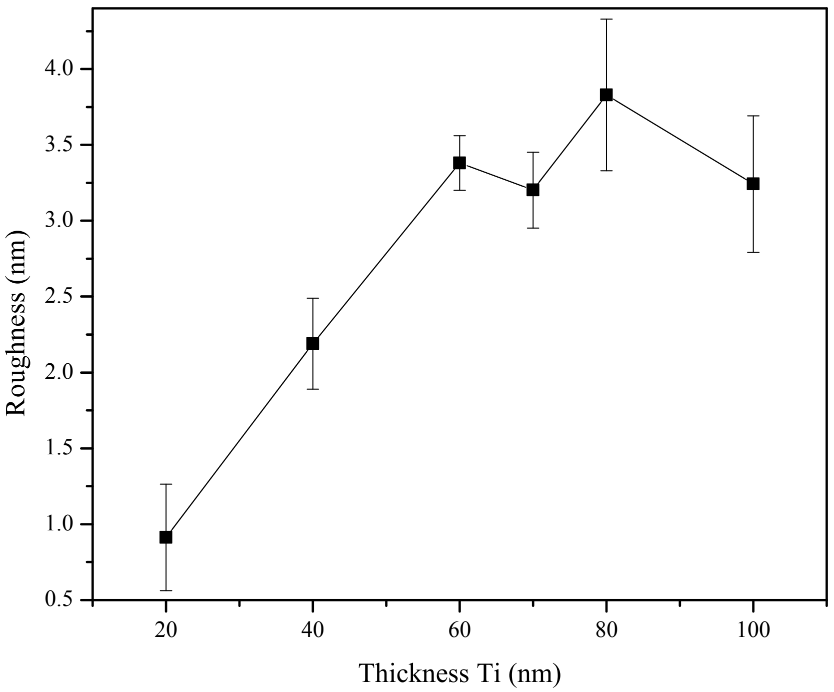

Figure 15. Trend of roughness measured for samples with constant thickness CoCrPt layers (*t* = 90nm) and varying thickness Ti layers. Lines connect points.

This increasing roughness likely is due to an increase in grain size[29]. As the underlayer thickness increases to a critical point (approximately *t* = 60nm), homogenous large grains are formed. A rougher surface results in more free poles and pinning sites, leading to a more complex domain structure. This new domain structure should result in increased coercivity (observed in Figure 13b) and broader SFD peaks (not observed in Figure 13f). Since the SFD values show no real trend, there is probably also a secondary reason for the increase in roughness as CoCrPt increases.

EFFECTS OF VARYING COCRPT FILM THICKNESS

After choosing the sample with the greatest inherent coercivity (Ti underlayer *t* = 80nm), several thicknesses of CoCrPt film (*t* = 50, 75, 90, 100, 125, 150) were fabricated and tested to investigate how the magnetic, crystallographic and topographical characteristics of the system change. For clarification, the results have been separated into three sections: magnetic properties, crystallography, and topography.

MAGNETIC PROPERTIES

The hysteresis loops obtained with a MicroSense VSM for samples of varying Ti thickness are presented in Figure 16 below:

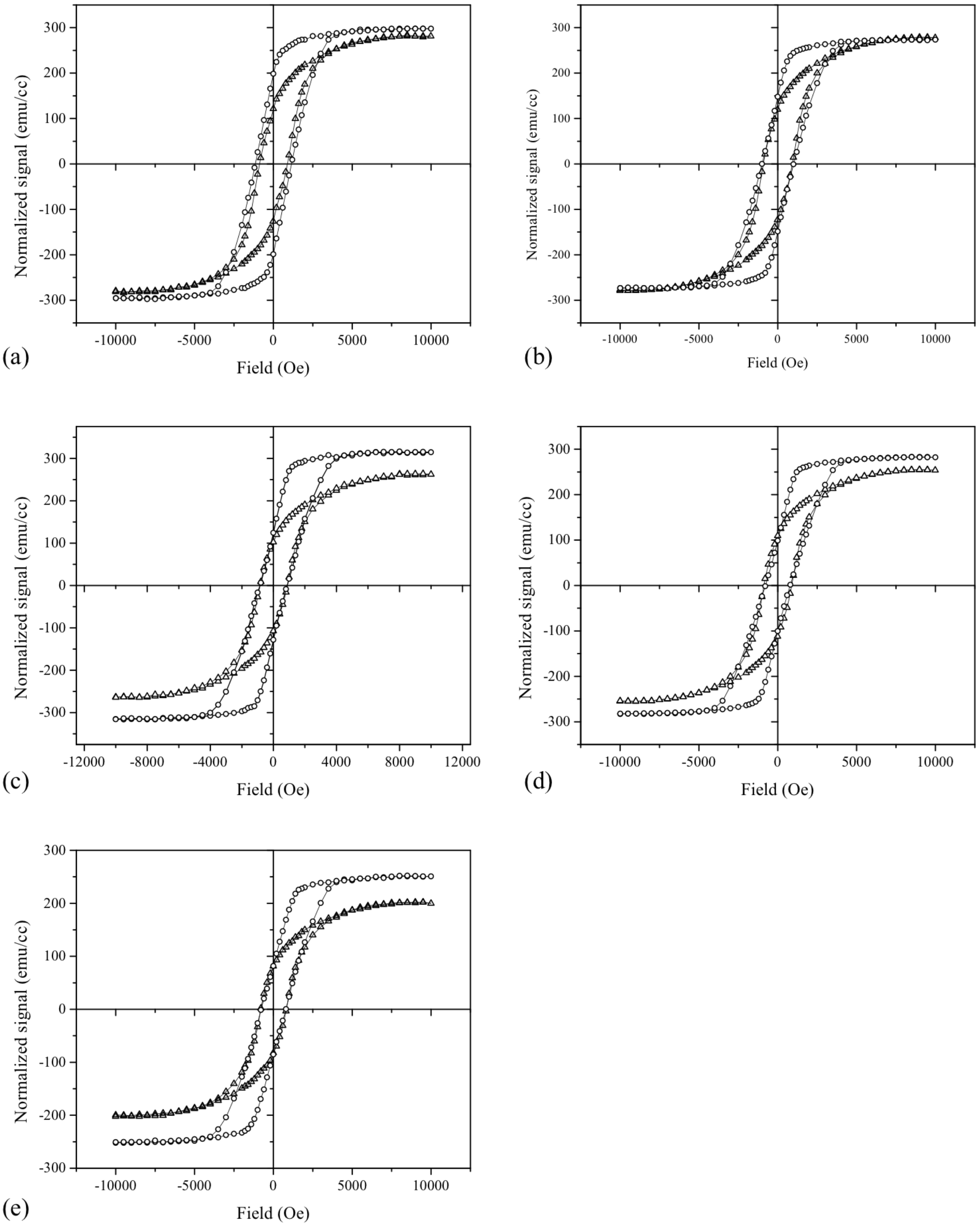

Figure 16. Out-of plane M-H curves for constant Ti underlayer (t = 80nm) with varying CoCrPt film thickness. In each graph, a circle (○) indicates out-of-plane loops and an upward facing

triangle (△) indicates the in-plane loops. CoCrPt thickness values are as follows (a) *t* = 50nm; (b) *t* = 75nm; (c) *t* = 100nm; (d) *t* = 125nm; (e) *t* = 150nm. Lines connect points.

Using the hysteresis loops in Figure 16, the magnetization saturation, coercivity, remanence, squareness, switching field distribution, and anisotropy energy density were calculated and are presented in Figure 17 as a function of CoCrPt film thickness.

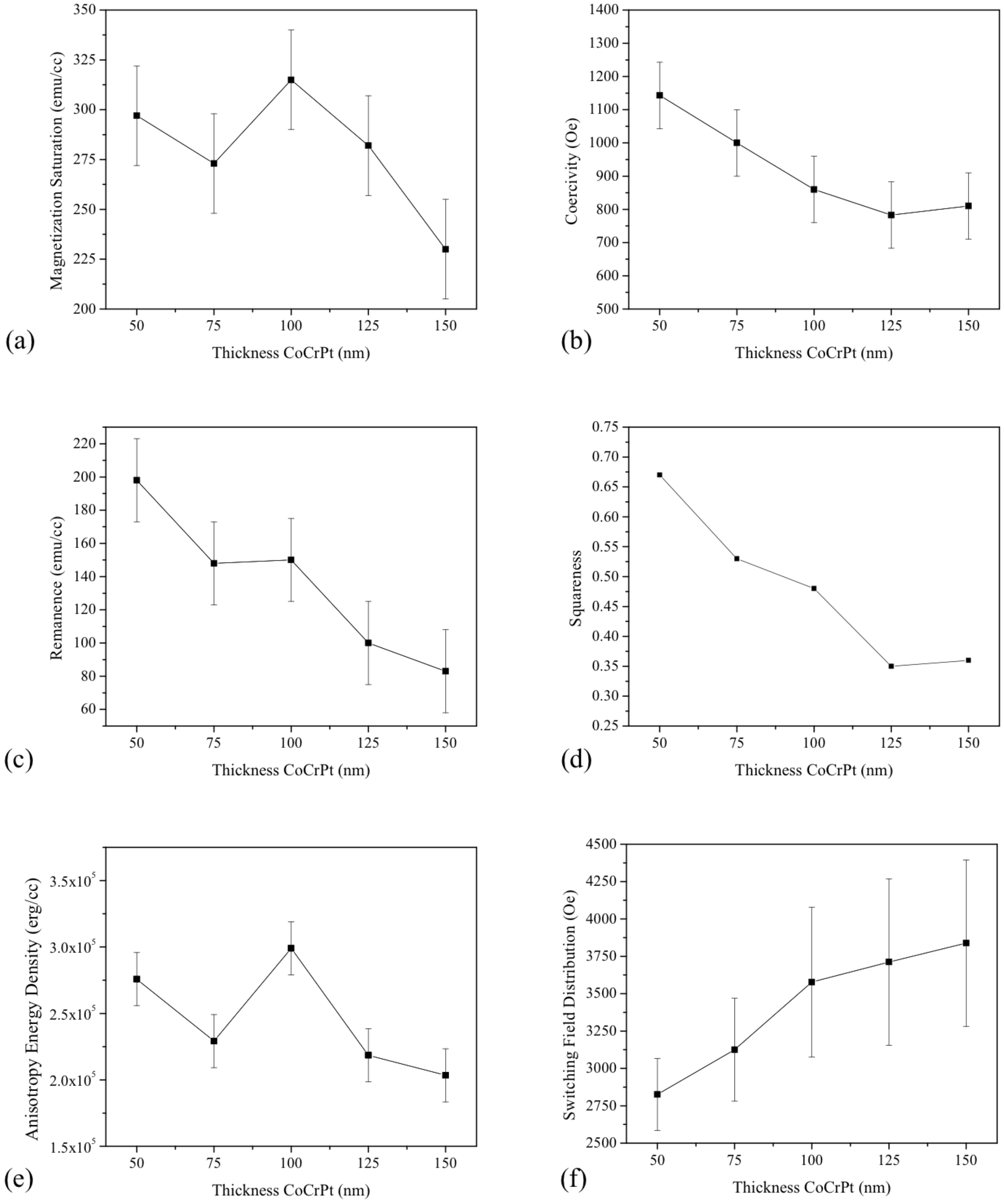

Figure 17. The out-of-plane magnetic properties of CoCrPt (*t* = 50, 75, 100, 125, 150nm) and constant Ti underlayer thickness (*t* = 80nm). The properties are as follows (a) magnetization

saturation (emu/cc), (b) coercivity (Oe), (c) remanence (emu/cc), (d) squareness, (e) anisotropy energy density (erg/cc); (f) switching field distribution (Oe). Lines connect points.

The out-of-plane magnetization saturation (Figure 17a) seems to show a slight downward trend, with a 25% decrease between *t* = 50nm and *t* = 150nm. The coercivity (Figure 17b) of the sample has a similar downwards trend, decreasing by a total of approximately 350 Oe. The remanence (Figure 17c) has a similar downward trend, decreasing from about 200 emu/cc to 80 emu/cc as the thickness of the CoCrPt film increases.

The squareness (Figure 17d) follows the trend of gradually decreasing as thickness of CoCrPt increases. The maximum value reported is 0.67 for *t* = 50nm with minimum values reported as 0.35 and 0.36 for *t* = 125nm and *t* = 150nm. The maximum values are nearly twice the minimum values. The anisotropy energy density (Figure 17e) seems to remain fairly constant. Though there is some fluctuation, the changes in values are minimal considering the inherent error and the small magnitude of the differences. The SFD (Figure 17f) shows a unique trend; it increases by about 1000 Oe total as the CoCrPt film thickness increases.

The slight downward trend in the magnetization saturation with increasing CoCrPt thickness is probably mostly due to errors in the estimation of the volume of the sample and step sizes used to measure these values. As was discussed above, since the material composition is constant, one would expect to see a consistent value for magnetization saturation. The coercivity also generally decreases which would make sense because as the film thickens, the uniaxial crystal organization is more likely to interrupted or shifted because of the method of fabrication, sputtering. There is also possibly relaxation of the lattice, which would be strained at the Ti-CoCrPt interface. The relaxation, which would be possible only in a sufficiently thick layer, would result in a change in the lattice parameters, which would in turn affect the strength of the magnetocrystalline anisotropy. Additionally, the rotation of moments is easier in a thicker film.

In a thin film, the rotation of magnetic moments incurs an energy penalty because it creates free poles on the surface. In a thicker film, this becomes easier, resulting in a decreased coercivity and remanence (see Figure 17b, c).

The remanence also shows a trend of decreasing as the film thickness increases. This is similarly explained by the increasing likelihood that the film will be less ordered as it gets thicker. A less perfectly ordered film would show a lower magnetization in the c-axis direction (out-of-plane) at a zero field. Likewise, a relaxation in the lattice as the thickness increases would result in a decrease in remanence. The squareness, like in the case with the changing Ti thickness, is dominated by the remanence since the magnetization saturation does change significantly over the range of CoCrPt thicknesses.

The anisotropy energy density increases and decreases, but seems to have a notable decrease of about one third of the maximum value. Again, this could be explained by a relaxation in the lattice leading to a decrease in the difference between the energy needed to align the magnetization on the easy or hard axis. The switching field distribution shows a steady increase, which implies that the homogeneity of the size of particles is increasing with increasing CoCrPt film thickness. The Gaussian fits used to describe data for varying CoCrPt thickness is presented below in Table 6.

Table 6. Gaussian fits used to calculate the switching field distribution of samples with varying CoCrPt film thicknesses. See Equation 7.

CoCrPt film thickness (nm)	*a*	*b*	*c*	R^2 *value*
50	0.18	1122	1697	0.97
75	0.15	912.8	1877	0.95
100	0.16	770.9	2148	0.93
125	0.14	650.4	2229	0.92
150	0.12	652.9	2316	0.96

The majority of these fits have $R^2 \geq 0.95$, indicating that a Gaussian is a good predictor for the behavior of the data. However, there is still some error inherent in the data presented because the fit is not a perfect match for the data.

CRYSTALLOGRAPHY

The texture of the samples was interrogated using a PANalytical X'Pert PRO XRPD X-ray diffractometer. Figure 18 presents the superimposed data from several samples with different CoCrPt film thickness.

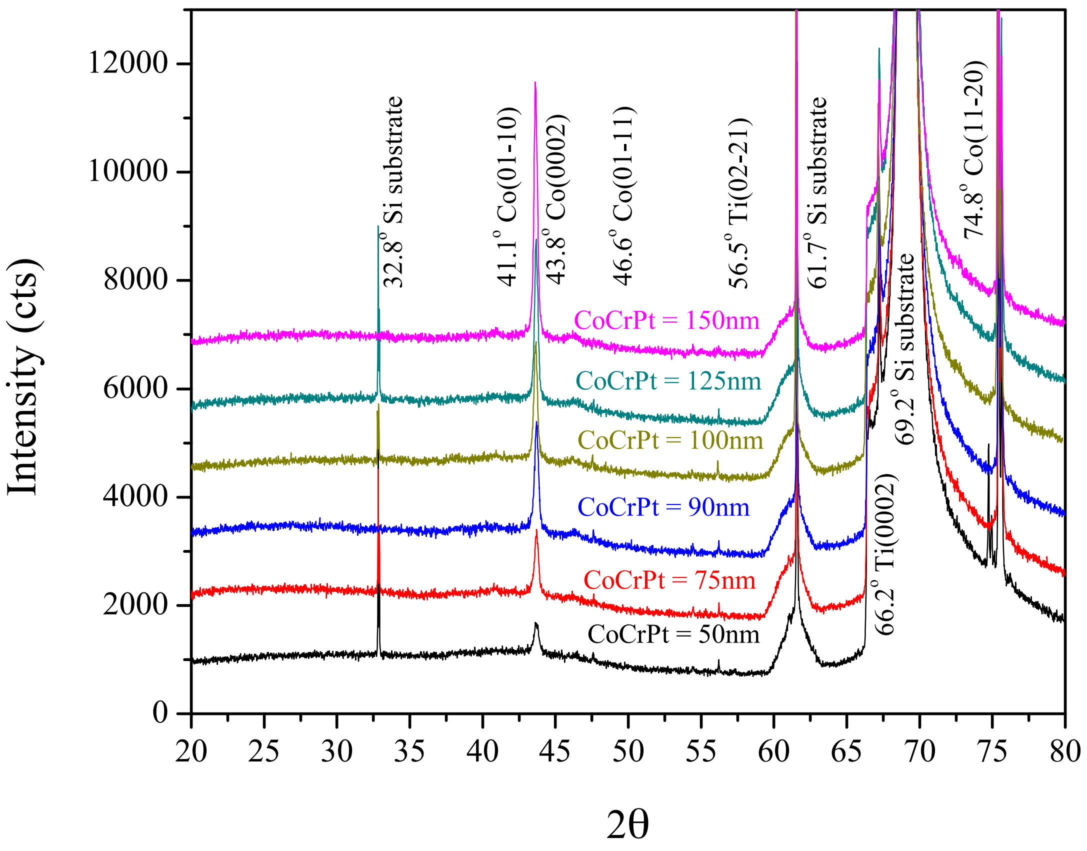

Figure 18. XRD scans for varying thickness CoCrPt films (*t* = 50, 75, 90, 100, 125, 150nm) and an 80nm Ti underlayer. Peaks identified using X'Pert Highscore software databases.

The labeled peaks in Figure 18 are present in at least one of the samples. The identification of these peaks was achieved with X'Pert Highscore software. The cobalt (0002) peaks appear to shift left as CoCrPt film thickness increases. The substrate peaks and the titanium peak do not appear to shift significantly.

The (0002) plane is present in all samples with variable CoCrPt peaks. The (11-20) plane only appears in the sample with a CoCrPt thickness of *t* = 50nm. The (01-11) plane also only appears in one sample (*t* = 150nm). The (01-10) peak appears in samples with thickness of *t* = 75, 100, and 150nm. Table 7 presents the relevant information for the (0002) peak identities for all samples.

Table 7. Crystallographic values acquired with XRD scans (step size 0.0167º) for varying CoCrPt underlayer thickness (t = 50, 75, 100, 125, 150nm). Values calculated with X'Pert Highscore software.

CoCrPt film thickness	*(0002) peak location (2θ)*	d (Å)	c (Å)	*FWHM*
50	43.64	2.074 ± 0.002	4.148 ± 0.002	0.1338 ± 0.008
75	43.68	2.072 ± 0.002	4.144 ± 0.002	0.2676 ± 0.008
100	43.65	2.073 ± 0.002	4.146 ± 0.002	0.2342 ± 0.008
125	43.66	2.073 ± 0.002	4.146 ± 0.002	0.2342 ± 0.008
150	42.61	2.075 ± 0.002	4.150 ± 0.002	0.2342 ± 0.008

With increasing thickness of the CoCrPt film, the (0002) peak generally shifts to lower values of 2θ. This trend is mirrored in the increase of d (calculated with Equation 8) and the increase of the lattice constant c. The values for FWHM are constant for t = 100, 125 and 150nm. When t = 50nm, the FWHM is much lower than would be expected and when t = 75nm, the FWHM has a slightly higher value than was observed for the other thicknesses.

This shifting of the peaks leads to, as was discussed above in the changing Ti thickness section, an increase in lattice constant (c) is expected. This increasing lattice constant should lead to a more elongated unit cell with a larger magnetocrystalline anisotropy than a unit cell with a shorter c lattice constant. Surprisingly, Figure 17e indicates a slight decrease in anisotropy with increasing thickness, implying that there are other factors that affect the anisotropy energy density beyond simply lattice constant.

The FWHM constant values for $t > 100$nm implies that there is no change in the c-axis dispersion of the samples. However, as will be discussed in the Conclusion, there are other methods to more accurately test this value that could help distinguish if there is any change due to CoCrPt film thickness. At t = 50nm, the FWHM has a lower value than the other samples, implying that there is less c-axis dispersion for this film thickness. At *t* = 75nm, the opposite is true, with a FWHM value that would imply a greater amount of c-axis dispersion than the other samples. Because these values do not support a trend with a clear motivation, these abnormalities are probably due to errors in the software calculation or lack of resolution on the peaks. Again, another method might be better suited to make a definitive statement about how the c-axis dispersion changes with the thickness of the CoCrPt film.

TOPOGRAPHY

With the Ti underlayer kept constant (*t* = 80nm), the thickness of the CoCrPt film may have an effect on the roughness of the sputtered film. The measured roughness of the films is presented in Figure 19.

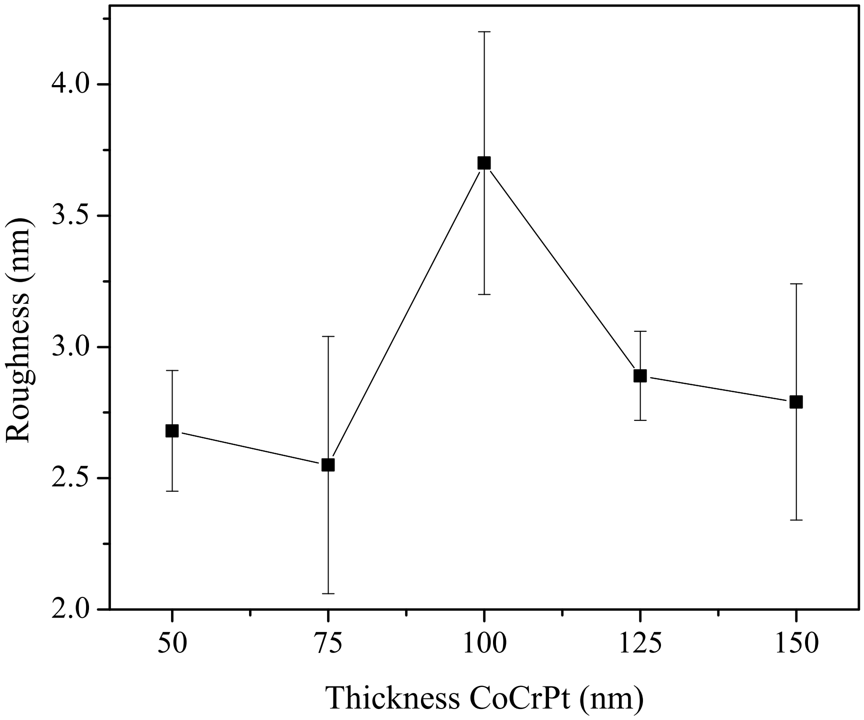

Figure 19. Trend of roughness measured for samples with varying thickness CoCrPt layers and constant thickness Ti layers (*t* = 80nm). Lines connect points.

As CoCrPt increases, the roughness of the samples appears to increase and then decrease. However, because the difference in the values is approximately within the bounds of the error due to the nature of the measurement, the roughness could be assumed to remain roughly constant with increasing film thickness. This implies that $t = 50$nm is thick enough to have overcome any inhomogeneity due to the sputtering of a very thin layer.

CONCLUSION AND FURTHER WORK

CoCrPt has many potential applications in memory storage because of its perpendicular magnetic anisotropy. The encouragement of this specific property through growth is often dependent on an underlayer to ensure hcp c-axis growth. This project investigated the inherent properties of the CoCrPt film fabricated, the effect of changing the thickness of a Ti underlayer, and the effect of changing the thickness of the CoCrPt magnetic film.

The composition of the fabricated samples was found to be $Co_{60.2}Cr_{16.4}Pt_{23.4}$, very different than the expected $Co_{66}Cr_{22}Pt_{12}$ given for the target. The increased platinum content could possibly explain why even CoCrPt film without an underlayer exhibited some PMA behavior. The Curie temperature of $Co_{60.2}Cr_{16.4}Pt_{23.4}$ is approximately 600 ºC where the out-of-plane hysteresis loop has obvious paramagnetic trends.

The addition of a Ti underlayer affects certain magnetic properties of CoCrPt ($t = 90$nm). As the thickness of the Ti increases to a critical value ($t \geq 60$nm), the coercivity also increases, reaching a maximum of about 1250 Oe. The remanence follows a similar trend, increasing to a maximum value of about 155 emu/cc. The anisotropy also seems to follow this trend, though the plateau above $t = 60$nm is less obvious. All of these patterns are likely caused by the widespread nucleation of c-axis oriented columnar grains in the Ti underlayer. Both the magnetization saturation and switching field distribution do not show a dependence on the thickness of the underlayer.

The XRD scans do not show a drastic change in the lattice parameter of the cobalt lattice as a function of the Ti underlayer and the fairly constant FWHM values imply an unchanging c-axis dispersion, though this could be studied in more detail. A notable exception is the $t = 20$ sample, which had a much wider FWHM, implying that that thickness of underlayer is perhaps insufficient to inspire homogenous out-of-plane growth. The topography of the CoCrPt film changes greatly with underlayer thickness—the roughness of the sample increases with increasing Ti underlayer, appearing to plateau, again, at $t = 60$nm. This increase is probably due to the formation of smaller grains, a theory supported by the similarly shaped increase in coercivity.

Studies were also completed with a fixed Ti underlayer thickness ($t = 80$nm) with variable thicknesses of CoCrPt magnetic films. The coercivity and remanence trend downward as CoCrPt film thickens, which could imply the relaxation of the lattice as the distance between the interface increases. The increase in the switching field distribution with increasing thickness suggests that having a thicker film increases the homogeneity of the grains in the sample. The anisotropy and magnetization saturation appear to be unaffected by alterations in the CoCrPt.

XRD scans show a trend of increasing lattice constant as the CoCrPt thickness increases, supporting the hypothesis that some relaxation of the lattice occurs in the thicker films. The roughness of the film stays fairly constant with increasing CoCrPt thickness.

In order to better understand the interactions between the Ti underlayer and the CoCrPt film, there are several more characterization methods that could be employed. As was mentioned above, a better study of the x-ray diffraction patterns could reveal important information.

Rocking curves would give a more exact value for FWHM and the distribution of grain orientation within the sample.

The films could also be cross-sectioned and observed with a TEM or SEM to try and observe the columnar grains. The films could also be studied using a selected area electron diffraction analysis on the TEM to ascertain how well aligned the CoCrPt crystal is in comparison to the Ti underlayer.

Additional work that could be performed is the observation how varying Ti or CoCrPt thickness affects the grain and domain size. The average grain size as well as the distribution of grain sizes could be observed with a scanning electron microscope and similar information could be obtained about the magnetic domains in the material using a magnetic force microscope. This information would complement the data collected on the magnetic properties, crystallography, and topography of CoCrPt with Ti underlayers.

WORKS CITED

[1] R.C. O'Handley, *Modern Magnetic Materials: Principles and Applications* (John Wiley & Sons, Inc., 2000).

[2] C.W. Chen, J. Mater. Sci. **26**, 3125 (1991).

[3] N. Inaba, A. Nakamura, T. Yamamoto, Y. Hosoe, and M. Futamoto, J. Appl. Phys. **79**, 5354 (1996).

[4] M.L. Plumer, J. van Ek, and D. Weller, editors , *The Physics of Ultra-High-Desnity Magnetic Recording* (Springer, New York, 2001).

[5] C.L. Yaws, *Yaw's Handbook of Properties of the Chemical Elements* (Knovel, 2011).

[6] H. Sato, T. Shimatsu, K. Mitsuzuka, T. OIkawa, O. Kitakami, S. Okamoto, H. Muraoka, H. Aoi, and Y. Nakamura, Nippon Oya Jiki Gakkaishi **29**, 427 (2005).

[7] M.-Y. Im, J.-R. Jeong, and S.-C. Shin, J. Magn. Magn. Mater. **286**, 442 (2005).

[8] M. Futamoto, Y. Hirayama, N. Inaba, Y. Honda, L. Ito, A. Kikuga, and T. Takeuchi, IEEE Trans. Magn. **35**, 2802 (1999).

[9] P. Glijer, J.M. Sivertsen, and J.H. Judy, J. Appl. Phys. **73**, 5563 (1993).

[10] C. Tsai, J. Liang, H.H. Liang, and C.M. Wang, J. Magn. Magn. Mater. **209**, 157 (2000).

[11] T. Keitoku, J. Ariake, N. Honda, K. Ouchi, and S. Iwasaki, J. Magn. Magn. Mater. **176**, 25 (1997).

[12] O. Kitakami, N. Kikuchi, S. Okamoto, Y. Shimada, K. Oikawa, Y. Otani, and K. Fukamichi, J. Magn. Magn. Mater. **202**, 305 (1999).

[13] M. Sago and T. Inoue, J. Appl. Phys. **67**, 6394 (1990).

[14] U.M. Gana, Int. J. Res. Rev. Appl. Sci. **17**, 370 (2013).

[15] H. Song, K.-H. Shin, and S.-J. Kwon, J. Magn. Magn. Mater. **226-230**, 1666 (2001).

[16] X. Liu, Z. Li, W. Shi, S. Li, F. Wei, D. Wei, and X. Liu, J. Appl. Phys. **105**, 07D503 (2009).

[17] C.L. Platt, K.W. Wierman, E.B. Svedberg, T.J. Klemmer, J.K. Howard, and D.J. Smith, J. Magn. Magn. Mater. **247**, 153 (2002).

[18] L. Tang, L. Lee, D.E. Laughlin, and D.N. Lambeth, Appl. Phys. Lett. **69**, 1163 (1996).

[19] H. Gong, M. Rao, D.E. Laughlin, and D.N. Lambeth, J. Appl. Phys. **85**, 4699 (1999).

[20] G. Choe, IEEE Trans. Magn. **31**, 2809 (1995).

[21] F. Gao, H. Sun, S. Feng, H. Yu, L. Jia, C. Pan, H. Zhou, X. Nie, and Y. Sun, Trans. Nonferrous Met. Soc. China **15**, 400 (2005).

[22] Y. Sonobe, Y. Ikeda, H. Uchida, and T. Toyooka, J. Appl. Phys. **81**, 4667 (1997).

[23] I.S. Lee, H. Ryu, H.J. Lee, and T.D. Lee, J. Appl. Phys. **85**, 6133 (1999).

[24] C.J. Sun, G.M. Chow, J.P. Wang, E.W. Soo, and J.H. Je, J. Appl. Phys. **93**, 8725 (2003).

[25] C.J. Sun, G.M. Chow, E.W. Soo, J.P. Wang, Y.K. Hwu, T.S. Cho, J.H. Je, H.H. Lee, J.W. Kim, and D.Y. Noh, J. Nanosci. Nanotechnol. **1**, 271 (2001).

[26] C.J. Sun, G.M. Chow, J.P. Wang, E.W. Soo, Y.K. Hwu, J.H. Je, T.S. Cho, H.H. Lee, and D.Y. Noh, J. Appl. Phys. **91**, 7182 (2002).

[27] C.J. Sun, J.P. Wang, E.W. Soo, and G.M. Chow, J. Appl. Phys. **95**, 7303 (2004).

[28] P. Jang, S. Hong, and J. Kim, J. Appl. Phys. **93**, 7741 (2003).

[29] M.A. Parker, K.E. Johnson, C. Hwand, and A. Bermea, IEEE Trans. Magn. **27**, 4730 (1991).

Picture Credit

Figure 1. http://hyperphysics.phy-astr.gsu.edu/hbase/audio/tape2.html

Figure 2. http://www.gitam.edu/eresource/Engg_Phys/semester_2/magnetic/magrecording.htm

Figure 3. http://www.ece.nus.edu.sg/isml/MRAM.jpg